buildings

MDPI

Article

Research on Energy-Saving Retrofit Optimization of Existing Multi-Story Residential Buildings in Suzhou, Anhui Province, China, Based on ANN Surrogate Models and Multi-Objective Optimization

Zhongcheng Duan, Shibo He, Zhou Hao and Leilei Wang *

School of Architecture and Design, China University of Mining and Technology, Xuzhou 221000, China; duanzhongcheng@cumt.edu.cn (Z.D.); ts24190023p31@cumt.edu.cn (S.H.); ts24190022p31@cumt.edu.cn (Z.H.)
* Correspondence: ts23190037p31@cumt.edu.cn; Tel.: +86-18439239223

Abstract

To address the trade-offs among energy savings, thermal comfort, and retrofit cost in existing multi-story residential buildings in cold climate regions, this study developed a retrofit optimization framework integrating building performance simulation, artificial neural network (ANN) surrogate models, and multi-objective optimization. A typical six-story residential building in Suzhou, Anhui Province, was selected as the case building. The DesignBuilder model was calibrated against one month of measured summer data, and the design variables were screened using Morris sensitivity analysis. Latin hypercube sampling was then employed to generate 5000 samples for training separate surrogate models of annual net electricity-use intensity (ANEUI), annual discomfort hours (DH), and initial retrofit cost per unit floor area (IRC). The optimization performance of NSGA-III, MOPSO, and NSGA-III-PSO was compared, and a compromise solution was identified using a combined subjective-objective weighting TOPSIS method. NSGA-III-PSO showed a better balance between convergence and objective-space coverage. EnergyPlus re-simulation indicated that the compromise solution reduced ANEUI from 60.29 to 35.98 kWh/(m^2·a) and DH from 5413.2 to 4012.5 h, corresponding to reductions of 40.3% and 25.8%, respectively, while the IRC was 398.9 CNY/m^2. The proposed framework provides quantitative decision support for integrated residential retrofits under comparable climatic conditions.

Keywords: existing multi-story residential building; energy-efficient retrofit; artificial neural network; multi-objective optimization; thermal comfort

Check for updates

Academic Editor: Ahmet Benli

Received: 10 September 2026
Revised: 26 October 2026
Accepted: 27 October 2026
Published: 6 November 2026

Copyright: © 2026 by the authors. Licensee MDPI, Basel, Switzerland. This article is an open access article distributed under the terms and conditions of the Creative Commons Attribution (CC BY) license.

1. Introduction

In the context of addressing climate change and promoting green and low-carbon development, improving the performance of existing residential buildings has become an important pathway for reducing energy consumption and enhancing indoor environmental quality in the building sector [1]. A large number of early-built multi-story residential buildings suffer from insufficient thermal performance of the building envelope, low energy efficiency, and unsatisfactory indoor thermal environments [2,3]. When the structural systems remain serviceable, performance-oriented retrofits can extend building service life while reducing resource consumption and construction waste associated with demolition and reconstruction. Suzhou, Anhui Province, contains a considerable number of four- to six-story residential buildings constructed from the 1990s to the early 2000s. These

buildings generally lack adequate external wall insulation, energy-efficient windows, and shading devices, with indoor environmental regulation during summer and winter relying mainly on occupant-installed equipment. Therefore, achieving a balance among energy consumption, thermal comfort improvement, and retrofit cost under limited investment remains a key challenge for the renovation of such existing residential buildings.

Previous studies have extensively investigated retrofit measures including wall and roof insulation, energy-efficient windows, shading systems, ventilation strategies, and energy systems. Wu et al. [4] demonstrated that coordinated retrofits of building envelopes and energy systems could improve residential energy and environmental performance. Jung et al. [5] evaluated multi-story residential retrofit strategies from energy, environmental, and economic perspectives. Tettey et al. [2] found that insulation, energy-efficient windows, and ventilation heat recovery could reduce operational energy consumption and mitigate overheating risks. Related studies in China have also indicated that integrated retrofits involving multiple building components generally outperform individual measures [3]. However, high-performance envelope components and renewable energy systems are often associated with higher initial investments, while indoor temperature control strategies may introduce trade-offs between energy consumption and thermal comfort. Therefore, evaluations based on a single performance indicator are insufficient to reveal the interactions and trade-offs among energy, comfort, and economic objectives.

Multi-objective optimization has gradually been applied to building performance optimization by identifying feasible boundaries among conflicting objectives through Pareto non-dominated solutions. Multi-objective particle swarm optimization (MOPSO) and the non-dominated sorting genetic algorithm II (NSGA-II) have been applied to residential energy-comfort optimization and building envelope design [6,7]. The non-dominated sorting genetic algorithm III (NSGA-III), which maintains solution diversity in multi-objective spaces through a reference-point mechanism, has also been adopted for comprehensive building performance optimization [8]. Hybrid algorithms that integrate different search mechanisms may improve convergence characteristics or search stability for specific optimization problems [9,10]. However, the performance of metaheuristic algorithms is highly problem-dependent, and different algorithms may produce different results under variations in variable dimensions, objective conflicts, and parameter settings. Therefore, comparing optimization algorithms under identical variable constraints and generation limits is more appropriate for evaluating their suitability for specific retrofit problems than directly adopting a single algorithm.

Building multi-objective optimization requires repeated evaluations of a large number of candidate solutions. Directly calling dynamic simulation tools such as EnergyPlus for each evaluation can result in considerable computational costs. Artificial neural networks (ANNs) can learn nonlinear mappings between retrofit variables and building performance indicators and have been widely applied for predicting energy consumption, thermal comfort, and economic performance [6,11,12]. Duan et al. [13] combined ANN and NSGA-III to investigate energy consumption, thermal comfort, and greenhouse gas emissions of multi-story residential buildings in Suzhou, Anhui Province, demonstrating the potential of surrogate models for multi-objective building optimization. Unlike that study, which optimized total energy demand, thermal discomfort, and life-cycle carbon emissions over 14 design variables and ranked the solutions by VIKOR, the present work optimizes annual net electricity-use intensity, annual discomfort hours, and initial retrofit cost over 26 variables, compares three optimization algorithms under identical conditions, and verifies the selected compromise solution by EnergyPlus re-simulation.

Accordingly, this study develops an integrated retrofit solution selection framework by combining building performance simulation, an ANN surrogate model and multi-

objective optimization for a typical existing six-story residential building in Suzhou, Anhui Province. The optimization objectives are annual net electricity-use intensity (ANEUI), annual discomfort hours (DH) and initial retrofit cost per unit floor area (IRC), and the decision variables cover operational control parameters, building envelope characteristics, energy-efficient windows, orientation-specific window-to-wall ratios (WWRs), external shading, vertical greening and rooftop photovoltaics.

The main contributions of this study are as follows:

1. Initial retrofit cost per unit floor area is optimized jointly with annual net electricity-use intensity and annual discomfort hours, so that the retrofit budget is traded off against the two performance targets inside the optimization rather than fixed in advance.
2. The decision space comprises 26 parameters, and NSGA-III, MOPSO and NSGA-III-PSO are applied to this same problem, and their Pareto fronts are compared by hypervolume and spacing.
3. The compromise solution selected by a combined subjective–objective weighting TOPSIS is returned to the calibrated model, where its ANEUI and DH are re-simulated and its initial cost, which the simulation does not provide, is recomputed from engineering quantities at four representative solutions.

2. Methodology

The research methodology consists of six stages: physical model development and calibration, parametric sample generation, ANN surrogate model training, multi-objective optimization, TOPSIS-based decision-making, and simulation-based assessment.

2.1. Research Framework

The overall workflow is illustrated in Figure 1, including six stages: physical model calibration, parametric sample generation, ANN surrogate model training, multi-objective optimization, TOPSIS decision-making, and simulation-based assessment. Regional surveys and on-site measurements were conducted to identify the case building and calibrate the simulation model. The ANN surrogate model trained using parametric simulation data was employed for rapid evaluation of candidate solutions, and the final compromise solution was returned to EnergyPlus for re-simulation.

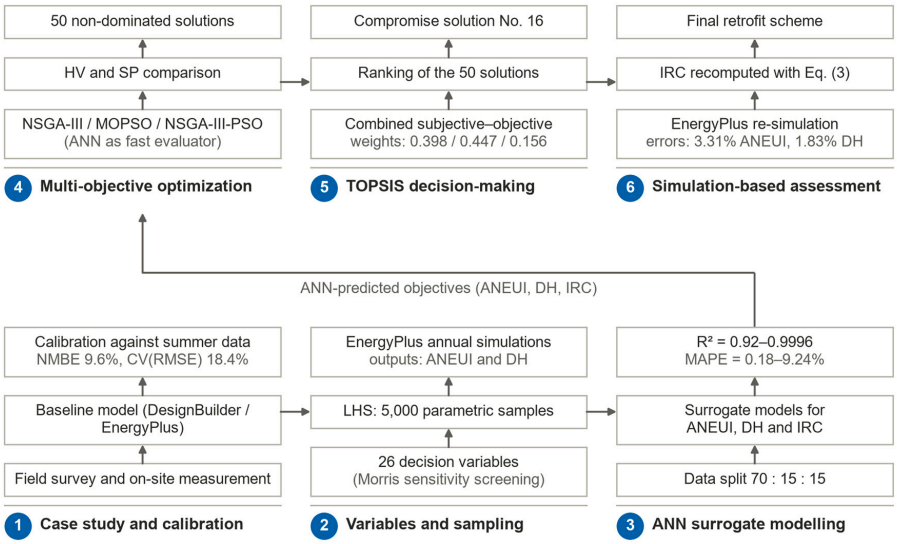


Figure 1. Research framework.

2.2. Performance Objectives and Retrofit Variables

2.2.1. Performance Objectives

In this study, the retrofit of the existing residential building was formulated as a multi-objective optimization problem involving 26 decision variables and three minimization objectives: ANEUI, DH, and IRC.

(1) annual net electricity-use intensity

Annual net electricity-use intensity (ANEUI) was defined as the annual building electricity demand offset by on-site photovoltaic generation and normalized by the total floor area. The building electricity demand was calculated as the sum of annual cooling, heating, lighting, and equipment electricity consumption. ANEUI was calculated as:

$$\mathrm{ANEUI} = \frac{E_{clg} + E_{htg} + E_{light} + E_{equip} - E_{PV}}{A_{total}} \quad (1)$$

where E_{clg}, E_{htg}, E_{light}, and E_{equip} represent the annual electricity consumption for cooling, heating, lighting, and equipment, respectively (kWh/a); E_{PV} represents the annual electricity generation of the rooftop photovoltaic system (kWh/a); and Atotal represents the total building floor area (m^2). ANEUI is therefore a net indicator for the retrofit package as a whole rather than a measure of the thermal performance of the envelope alone, because the retrofit packages combine demand-side measures with rooftop photovoltaic generation and the electricity purchased by the building is determined by the annual balance between on-site demand and on-site generation.

(2) Annual discomfort hours

Indoor thermal comfort was evaluated using the Fanger PMV–PPD model with reference to ISO 7730:2025 [14]. The acceptable PMV comfort interval was defined as $-0.5 \leq \mathrm{PMV} \leq +0.5$. A simulation timestep was classified as uncomfortable when $\mathrm{PMV} < -0.5$ or $\mathrm{PMV} > +0.5$. Therefore, both cold and heat discomfort were included in the calculation of annual discomfort hours.

Annual discomfort hours were calculated as:

$$\mathrm{DH} = \Sigma t = 1\mathrm{TI}(\mathrm{PMVt} < -0.5 \text{ or } \mathrm{PMVt} > +0.5)\Delta t \quad (2)$$

where $I(\cdot)$ is an indicator function that equals 1 when the PMV value falls outside the acceptable comfort interval and 0 otherwise; Δt is the simulation timestep; and T is the total number of annual simulation timesteps. In the present model, the EnergyPlus simulation timestep was 10 min, corresponding to $\Delta t = 1/6$ h. The same PMV comfort interval, timestep, and aggregation procedure were applied to both the baseline and retrofit cases.

(3) Initial retrofit cost per unit floor area

The economic objective was defined as the initial retrofit cost per unit floor area (IRC):

$$\mathrm{IRC} = \frac{C_{env} + C_{win} + C_{vg} + C_{PV} + C_{fix}}{A_{total}} \quad (3)$$

where C_{env} represents the costs of insulation for external walls, roofs, and floors; C_{win} represents the costs of windows and shading systems; C_{vg} represents the cost of vertical greening; C_{PV} represents the cost of the photovoltaic system; and C_{fix} represents fixed costs associated with high-altitude operations, equipment rental, and other construction measures. The envelope, window, and shading components were priced from the retrofit quantities and the corresponding unit prices of the selected products, whereas C_{vg} and C_{PV} were derived from the categorized vertical greening systems and photovoltaic configurations listed in Tables A3 and A4, respectively, in which each system type or configuration is associated with its own unit cost. IRC therefore represents only the one-time investment at the retrofit implementation stage and excludes operational energy costs, equipment depreciation, and long-term maintenance costs.

2.2.2. Retrofit Variables

The retrofit variables were determined based on regional residential surveys, building thermal performance principles, relevant standards, and available product performance ranges [15–18]. Table 1 summarizes the 26 decision variables, their baseline values, and the search ranges adopted for the retrofit alternatives. The baseline values describe the existing building, which was simulated separately as the reference case, whereas the search ranges define the retrofit configurations considered in the optimization. These ranges therefore do not necessarily include the corresponding baseline values. For example, the retrofit ranges specify greater insulation thicknesses and lower window U-values and solar heat gain coefficients than the baseline values, while zero baseline values for shading depth, plant layer thickness and photovoltaic coverage ratio indicate the absence of these measures in the existing building.

Table 1. Retrofit decision variables and value ranges.

Category	Description	Variable	Data Type	Baseline Value	Retrofit Search Range	Unit
Air-conditioning setpoint temperature	Cooling setpoint temperature	P1	Continuous	26	[23–28]	°C
	Heating setpoint temperature	P2	Continuous	18	[18–27]	°C
Insulation thickness	Roof MW insulation material	P3	Continuous	0.05	[0.12–0.2]	m
	North wall XPS insulation material	P4	Continuous	0.03	[0.12–0.26]	m
	South wall XPS insulation material	P5	Continuous	0.03	[0.12–0.26]	m
	West wall XPS insulation material	P6	Continuous	0.03	[0.10–0.22]	m
	East wall XPS insulation material	P7	Continuous	0.03	[0.10–0.22]	m
	Floor XPS insulation material	P8	Continuous	0.03	[0.04–0.1]	m
Window U-value	North window U-value	P9	Continuous	2.7	[1.5–2.5]	$W/m^2 \cdot K$
	South window U-value	P10	Continuous	2.7	[1.5–2.5]	$W/m^2 \cdot K$
Window solar heat gain coefficient (SHGC)	North window SHGC	P11	Continuous	0.7	[0.30–0.45]	-
	South window SHGC	P12	Continuous	0.7	[0.45–0.6]	-
XPS insulation thermal conductivity	North wall XPS thermal conductivity	P13	Continuous	0.03	[0.029–0.035]	W/m·K
	South wall XPS thermal conductivity	P14	Continuous	0.03	[0.029–0.035]	W/m·K
	West wall XPS thermal conductivity	P15	Continuous	0.03	[0.029–0.035]	W/m·K
	East wall XPS thermal conductivity	P16	Continuous	0.03	[0.029–0.035]	W/m·K
Vertical greening	Plant layer solar absorptance	P17	Continuous	0	[0.3–0.9]	-
	Plant layer thickness	P18	Continuous	0	[0.05–0.3]	m
Photovoltaic system	Photovoltaic tilt angle	P19	Continuous	0	[0–60]	°
	Photovoltaic coverage ratio	P20	Continuous	0	[20–85]	%
External shading	Shading depth	P21	Continuous	0	[0.2–1.2]	m
Building airtightness	Air change rate	P22	Continuous	1.0	[0.5–1.5]	h^{-1}
Window-to-wall ratio (WWR)	South window-to-wall ratio	P23	Continuous	31	[25–55]	%
	North window-to-wall ratio	P24	Continuous	25	[20–40]	%
	East window-to-wall ratio	P25	Continuous	8.5	[5–30]	%
	West window-to-wall ratio	P26	Continuous	8.9	[5–30]	%

For clarity, the 26 decision variables were grouped according to their implementation characteristics. Relatively straightforward retrofit measures included insulation thickness and material properties, window U-values and solar heat gain coefficients, external shading, and building airtightness. Measures requiring substantial architectural or building-services intervention included vertical greening, rooftop photovoltaic tilt and coverage, and orientation-specific window-to-wall ratios. Cooling and heating setpoint temperatures were classified as operational control variables because they primarily represent adjustments to building operation rather than physical modifications to the building fabric. This classification distinguishes physical retrofit measures from operational adjustments when interpreting the optimization results.

During the sensitivity analysis stage, window height and window width in different orientations were converted into WWRs for four orientations in the final optimization process to improve engineering interpretability. Continuous variables were searched within their predefined boundaries, while discrete variables were represented using specified levels. Candidate solutions exceeding the feasible domain were corrected according to boundary constraints.

2.2.3. Sensitivity Analysis

Before surrogate model training, Morris global sensitivity analysis was employed to evaluate the relative influence of candidate variables on ANEUI and DH [19,20]. Since IRC was calculated based on engineering quantities and unit costs, its response mechanism differed from building thermal processes; therefore, it was not considered as an output in this sensitivity analysis stage. The Morris method quantifies variable effects by perturbing individual inputs and calculating elementary effects (EE):

$$EE_i = \frac{Y(\mathbf{x} + \Delta \mathbf{e}_i) - Y(\mathbf{x})}{\Delta} \quad (4)$$

where Y represents the model output, x represents the input vector, e_i represents the unit vector in the i-th direction, and Δ represents the perturbation step size in the normalized space. μi* represents the mean of the absolute elementary effects and is used to evaluate the overall influence intensity. σi represents the standard deviation of the elementary effects and reflects nonlinear effects or variable interactions. The sensitivity results were used for variable ranking, adjustment of the variable system, and interpretation of optimization results.

The screening covered k = 27 candidate variables, comprising the 26 design variables in Table 1 and the thermal conductivity of the planting substrate. A Morris design with p = 4 levels and r = 20 Latin-hypercube trajectories gave $\Delta = p/[2(p-1)] = 2/3$ and $N = r(k+1) = 560$ model evaluations. The standard error of μi* was approximated as $\sigma i/\sqrt{r}$, and the 95% confidence interval of μi* was estimated as $\mu i^* \pm t(0.975, r-1)\sigma i/\sqrt{r}$; with r = 20 and $t(0.975, 19) = 2.093$, the half-width of the interval is approximately $0.468\sigma i$. These intervals are approximate, because the elementary effects generated along Morris trajectories are not necessarily independent or normally distributed. Because ANEUI and DH are expressed in different units, μi* was normalised within each objective before the variables were ranked, and those needed to reach 99% of the cumulative root-sum-square contribution were classified as influential, while variables outside this limit for both objectives were excluded from the subsequent optimisation.

2.3. Surrogate-Assisted Multi-Objective Optimization

2.3.1. ANN Surrogate Model

To avoid frequent calls to building performance simulation during the iterative optimization process, a feedforward backpropagation ANN was adopted to establish surrogate relationships between the 26 retrofit variables and the three performance objectives [11,21].

After random shuffling, the parametric samples were normalized to [0,1] using the min-max normalization method:

$$x_i' = \frac{x_i - x_{i,min}}{x_{i,max} - x_{i,min}} \quad (5)$$

where x_i and x_i' represent the original and normalized values of the variables, respectively; $x_{i,min}$ and $x_{i,max}$ represent the minimum and maximum values in the sample dataset.

We generated 5000 parametric samples using Latin hypercube sampling and randomly divided them into training, validation, and testing sets at a ratio of 70:15:15. We used the training set to update the network weights, the validation set to compare candidate hidden neurons for the ANEUI, DH, and IRC surrogate models, and the testing set to evaluate the final generalization performance.

We developed three independent ANN surrogate models for ANEUI, DH, and IRC because the three objectives have different scales and response characteristics. Each model used the 26 retrofit variables as inputs and adopted a single-hidden-layer feedforward architecture with sigmoid activation in the hidden layer and linear output nodes, and the network weights were optimized using the Levenberg–Marquardt algorithm. Candidate hidden-neuron numbers were tested independently for the three models, and we selected 25, 35, and 5 hidden neurons for the ANEUI, DH, and IRC models, respectively, on the basis of the validation-set performance. Figure A3 compares the prediction accuracy obtained with different numbers of hidden neurons, and Figure A4 reports the training performance and learning parameters of the three selected models.

The prediction performance of the ANN surrogate models was evaluated using the coefficient of determination (R^2), root mean square error (RMSE), and mean absolute percentage error (MAPE) [22]. R^2 was used to assess the ability of the models to explain variations in the target variables, RMSE quantified the overall deviation between predicted and simulated values, and MAPE reflected the relative prediction error. Higher R^2 values and lower RMSE and MAPE values indicate better prediction accuracy of the surrogate models.

2.3.2. Coupling ANN with Optimization Algorithms

After training, the three ANN models were integrated into the objective evaluation functions of the multi-objective optimization algorithms. Candidate solutions were generated within the 26-dimensional feasible domain, normalized according to the training procedure, and evaluated using the three ANN models to obtain predicted values of ANEUI, DH, and IRC. These predictions were then used for non-dominated sorting, particle updating, and genetic operations.

NSGA-III selects solutions by non-dominated sorting, retains complete fronts, and truncates the last accepted front to the population size [23]. MOPSO approaches the Pareto front through particle position and velocity updates with an external archive [24]. NSGA-III-PSO incorporates particle swarm updating mechanisms into the NSGA-III sorting framework to balance global exploration and local exploitation. The main algorithm settings are summarized in Table 2.

The two mechanisms share a single population. In each generation the current non-dominated solutions of that population form the pool from which a global guide gi is drawn at random for each individual i. With xi(t) the position of individual i in generation t, pi its personal-best position, vi(t) its velocity, and r1 and r2 independent random vectors drawn uniformly from [0, 1] 26, the velocity and the PSO offspring are updated as $vi(t+1) = w(t)vi(t) + c1r1 \odot (pi - xi(t)) + c2r2 \odot (gi - xi(t))andyi = xi(t) + vi(t+1)$, where ⊙ denotes the element-wise product, c1 = c2 = 1.5, vi(0) = 0, and w(t) decreases linearly from 0.9 at the first generation to 0.4 at the last. A second offspring set is generated from the same parents

by simulated binary crossover (probability 0.9, distribution index 21) and polynomial mutation (probability 1/26 per variable, distribution index 21). Parents and both offspring sets are combined, truncated to the variable bounds, evaluated by the three ANN models, and reduced to 200 individuals by non-dominated sorting, complete fronts being kept and the last truncated to the remaining capacity; pi is replaced by the retained position whenever the latter dominates it. The hybrid thus evaluates 2nPop new candidates per generation, twice that of the other two algorithms.

Table 2. Main parameters of optimization algorithms.

Category	Parameter	Symbol	Setting/Strategy	Configuration Logic/Description
General parameters	Population size	nPop	200	Determines the coverage density of the search space
	Maximum number of iterations	MaxIt/maxGen	600	Uses a unified number of evolutionary generations to ensure sufficient convergence
	Decision variable dimension	nVars	26	Corresponds to the number of building design parameters
	Objective function dimension	nObj	3	ANEUI, DH, and IRC
	Number of extracted solutions	-	50	Uniform sample size used for performance comparison
MOPSO	Archive size	nArchive	150	Size of the external archive for storing non-dominated solutions
	Inertia weight	w	0.5	Balances global exploration and local exploitation
	Cognitive learning factor	c1	1.5	Degree to which particles follow their own historical best experience
	Social learning factor	c2	2	Degree to which particles follow leaders in the archive
NSGA-III	Crossover operator	-	Intermediate	Intermediate crossover to promote genetic recombination
	Mutation operator	-	Adaptive Feasible	Adaptive mutation to maintain engineering feasibility
NSGA-III-PSO	Inertia weight	w	0.9 → 0.4 (linearly decreasing)	Decreases progressively with iterations
	Cognitive learning factor	c1	1.5	Individual cognitive weight in the hybrid strategy
	Social learning factor	c2	1.5	Social cooperation weight in the hybrid strategy

The three algorithms adopted identical population sizes, iteration numbers, and variable constraints. After each run, the final non-dominated solution set was retained, and 50 representative Pareto solutions were extracted for performance comparison and decision analysis.

2.3.3. Evaluation of Optimization Algorithm Performance

The optimization performance was evaluated using the Pareto front, hypervolume (HV), and spacing (SP) indicators [25]. HV represents the volume of the objective space covered by the non-dominated solution set relative to a unified reference point, with larger values indicating better convergence and coverage performance. SP describes the dispersion of distances between adjacent non-dominated solutions, with smaller values indicating a more uniform distribution.

HV and SP were calculated after normalizing ANEUI, DH, and IRC, using the same reference point for all algorithms. The optimization performance was comprehensively evaluated based on indicator values, three-dimensional Pareto fronts, and two-dimensional objective projections.

2.4. Multi-Criteria Decision-Making and Simulation-Based Assessment

2.4.1. Combined Weighting TOPSIS

All solutions in the Pareto set are non-dominated, and a unique implementation scheme cannot be determined solely based on dominance relationships. Therefore, the combined subjective-objective weighting TOPSIS method was adopted to rank candidate solutions [26,27]. Assuming that the Pareto solution set contains n solutions and three evaluation indicators, all of which are of the cost type, each indicator was first normalized by the maximum of its column and expressed as a benefit-type value, so that a larger value indicates a better performance:

$$v_ij = \left(x_j^{max} - x_ij\right)/x_j^{max} \quad (6)$$

The objective weights were determined using information entropy, while the subjective weights were assigned according to the relative importance of energy performance, thermal comfort, and initial investment as ws = (0.4, 0.4, 0.2). Equal subjective priority was assigned to energy performance and thermal comfort, while initial investment received a lower weight. This choice was intended to prevent the larger dispersion of IRC from dominating an entropy-only decision and to retain the retrofit objective of jointly improving energy performance and comfort. These values were adopted as the baseline decision preference of this case rather than as universal weights; the entropy values of the three indicators were (0.9642, 0.9554, 0.9899), the corresponding objective weights were (0.396, 0.493, 0.111), and the two types of weights were combined by linear weighting with $\lambda = 0.5$:

$$w_j = \lambda w_j^s + (1 - \lambda) w_j^o \quad (7)$$

where w_j^s, w_j^o, and w_j represent the subjective weight, objective weight, and combined weight of the j-th indicator, respectively. Since Equation (6) expresses all three objectives as benefit-type values, the maximum value of each column constitutes the positive ideal solution, while the minimum value constitutes the negative ideal solution. The relative closeness of solution i was calculated as:

$$\mathrm{Ci} = \mathrm{Di,neg}/(\mathrm{Di,pos} + \mathrm{Di,neg}) \quad (8)$$

where Di,pos and Di,neg represent the Euclidean distances between solution i and the positive and negative ideal solutions, respectively. A larger Ci indicates that the solution is closer to the positive ideal solution. The solution with the highest relative closeness was selected as the compromise solution.

2.4.2. EnergyPlus Re-Simulation of the Selected Compromise Solution

To assess the ANN predictions at the selected design point, the 26 design variables of the TOPSIS-selected compromise solution were entered into the calibrated DesignBuilder model, and ANEUI and DH were recalculated using EnergyPlus. The weather data and non-optimized boundary conditions were consistent with those used to generate the parametric simulation samples. This procedure compares the surrogate predictions with the underlying simulation model for one selected solution; it does not constitute independent experimental or field validation.

The relative error between ANN predictions and re-simulation results was calculated as:

$$\varepsilon y = |\mathrm{ysim} - \mathrm{yANN}|/\mathrm{ysim} \times 100\% \quad (9)$$

where ysim denotes the EnergyPlus re-simulation result, yANN denotes the corresponding ANN prediction, and εy denotes the relative error. This comparison assesses agreement between the ANN predictions and the underlying building simulation model at the selected

compromise solution only. It does not constitute independent experimental or field validation, nor does it establish the accuracy of the entire optimized solution set. Performance improvements relative to the simulated baseline are determined from the re-simulation results under the adopted boundary conditions.

3. Case Study

3.1. Regional Survey and Case Building

Suzhou, Anhui Province (33.6° N, 116.9° E), is located in the northern part of Anhui Province and is classified as a cold climate region according to the Chinese Design Code for Thermal Performance of Civil Buildings (GB 50176-2016). The local climate is characterized by cold winters and hot, humid summers. Therefore, retrofit strategies for existing residential buildings should simultaneously consider winter heat preservation, summer heat protection, and solar heat gain control.

A regional survey was conducted from 16 July to 16 August 2025, covering Yongqiao District, Dangshan County, Lingbi County, Xiao County, and Sixian County. Design and technical information from 50 residential communities were initially collected, and three representative residential communities were selected from each administrative region for field investigation, resulting in 15 survey samples. The investigation mainly included building morphology, envelope characteristics, equipment usage, and resident questionnaires. Detailed building surveys and thermal environment measurements were further conducted for selected typical residential buildings. A total of 120 questionnaires were distributed, of which 110 valid responses were obtained. The basic characteristics of the surveyed buildings and the investigated envelope conditions are summarized in Tables 3 and 4, respectively. The questionnaire covered respondent characteristics, perceived indoor temperature, humidity, ventilation and noise, daily heating and cooling behavior, and willingness and cost acceptance for retrofit. Thermal sensation was recorded using the ASHRAE seven-point scale. Reliability and sampling suitability were assessed using Cronbach's α and the Kaiser–Meyer–Olkin (KMO) statistic: α and KMO were 0.838 and 0.832 for the summer questionnaire and 0.814 and 0.827 for the winter questionnaire, respectively.

Table 3. Summary of basic information on multi-story residential buildings.

Item	Type	Number of Buildings	Proportion (%)
Structural type	Reinforced concrete frame structure	12	24
	Masonry structure	38	76
Plan configuration	Linear layout	46	92
	L-shaped layout	3	6
	Others	1	2
Building storeys	4 storeys	15	30
	5 storeys	15	30
	6 storeys and above	20	40
Building floor area	≤100 m^2	20	40
	100–200 m^2	25	50
	>200 m^2	5	10
Construction period	Before 2000	8	16
	2000–2010	15	30
	2011–2020	18	36
	After 2021	9	18
Building orientation	South-facing	45	90
	Other orientations	5	10

Table 4. Summary of investigation results on enclosure structures.

Item	Material	Number of Buildings	Proportion (%)
Wall material	Masonry wall	28	56
	Autoclaved aerated concrete block	15	30
	Lightweight composite wall panel	7	14
Window and door material	Aluminum alloy	35	70
	Plastic-steel	15	30
Roof type	Flat roof	20	40
	Pitched roof	30	60
Roof material	Cast-in-place concrete	34	68
	Prefabricated slab	16	32
Floor material	Ceramic tile flooring	30	60
	Composite wood flooring	20	40

The surveyed residential buildings were mainly characterized by masonry structures and linear ("I-shaped") layouts, with building heights concentrated between four and six floors. Most buildings exhibited insufficient external wall insulation, while aluminum alloy or plastic-steel framed windows were commonly used, and systematic external shading systems were rarely installed. The survey results further indicated that split-type air-conditioning systems were the primary equipment used by residents for indoor environmental regulation during summer and winter, with usage rates of 68% and 50%, respectively. Thermal comfort satisfaction was lower in summer than in winter, suggesting that cooling, ventilation, and shading conditions during high-temperature periods require further improvement. The survey responses were further aggregated by season, and Figure A1 presents the distribution of the occupants' indoor environmental perceptions and satisfaction ratings, complementing the summer–winter comparison above by showing how the individual response categories were distributed in each season.

Considering building characteristics, measurement conditions, and data availability, a six-story brick-concrete structure residential building located in the Taoyuanju residential community, Dangshan County, was selected as the case building. The building appearance is shown in Figure 2. The building adopts a two-staircase and four-unit layout, containing 24 apartments with a total floor area of 1194 m^2. The standard floor height is 3.3 m. The living rooms and master bedrooms are arranged on the south side, while kitchens and secondary bedrooms are located on the north side. Its building form, functional layout, and envelope characteristics are highly consistent with the typical residential patterns identified in the regional survey. The building is approximately 33.0 m long and 10.6 m wide.



(a) (b)

Figure 2. Appearance of the case building: (**a**) south facade; (**b**) north facade.

3.2. Baseline Model and On-Site Measurement

The baseline model was developed using DesignBuilder, and EnergyPlus was employed for building thermal and energy performance simulations, as illustrated in Figure 3. Building geometry, spatial zoning, envelope properties, and operational parameters were defined based on field measurements, construction surveys, and resident usage patterns. Repeated residential units were appropriately simplified while maintaining consistency in total floor area, orientation, external surface area, and major functional space relationships. Annual simulations were conducted using the typical meteorological year EPW file for Suzhou, Anhui Province.

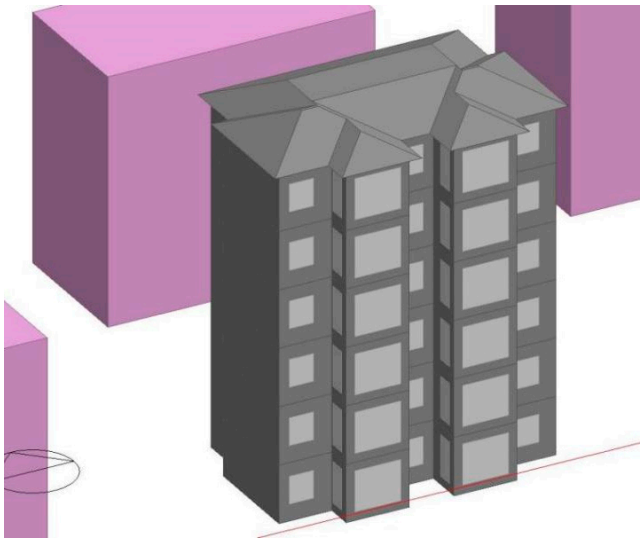


Figure 3. Baseline model of the case building.

For the thermal comfort assessment, the PMV–PPD calculation settings are summarized in Table 5. The same settings were applied to the baseline and retrofit cases to ensure a consistent comparison of annual discomfort hours. The model used summer and winter clothing schedules, with the corresponding seasonal settings applied through the EnergyPlus schedule throughout the annual simulation. No additional clothing category was introduced for the transitional seasons.

Table 5. PMV and DH calculation settings used in the annual simulations.

Parameter	Setting
PMV model	Fanger PMV–PPD
Standard	ISO 7730:2025 [14]
Acceptable PMV interval	−0.5 to +0.5
Indoor air velocity	0.10 m/s
Mean radiant temperature	Calculated by DesignBuilder–EnergyPlus from zone thermal conditions
Metabolic rate	1.0 met
Summer clothing	0.5 clo
Winter clothing	0.9 clo
Annual weather boundary	Suzhou typical meteorological year EPW

The envelope and window parameters of the baseline building are summarized in Tables 6 and 7, respectively. The external wall consists of a combination of brick masonry and concrete blocks, with the existing configuration including a 30 mm XPS insulation layer. The roof comprises a 50 mm mineral wool insulation layer and a 150 mm concrete slab, while the floor incorporates a 30 mm XPS insulation layer. The baseline windows consist of 5 mm clear single glazing with aluminum alloy frames. The HVAC system was represented using an ideal loads air system, with cooling and heating setpoints of 26 °C and 18 °C, respectively. The room-level operating and internal load parameters that define the simulation boundary conditions, including the air-conditioned rooms, the winter and summer design temperatures and relative humidities, the illuminance levels, and the lighting and equipment power densities, are summarized in Table A2 and were applied identically to the baseline and all parametric simulations.

Table 6. Thermal properties of the baseline building envelope.

Building Envelope	Material	Thickness (mm)	Thermal Conductivity (W/m·K)	Density (kg/m^3)	Specific Heat Capacity (J/kg·K)
Roof	Asphalt waterproofing layer	10	-	-	-
	MW insulation layer	50	0.035	30	100
	Air cavity	20	0.024	1.225	1005
	Concrete floor slab	150	1.2	2200	860
	Gypsum finish layer	12	0.17	800	1200
Wall	Cement plaster layer	15	0.75	1300	800
	Brick masonry wall	100	0.7	1500	800
	XPS insulation layer	30	0.03	30	1500
	Concrete block	100	1.2	2200	850
	Gypsum plaster layer	10	0.2	700	1000
Floor	XPS insulation layer	30	0.03	30	1500
	Cast concrete	100	1.2	2200	850
	Floor leveling layer	70	0.8	1500	1000
	Wood flooring	30	0.15	500	1500

Table 7. Window parameters of the baseline building.

Material	Thickness	Thermal Conductivity (W/m·K)	Visible Transmittance	Solar Heat Gain Coefficient (SHGC)
Clear glass	5	1	0.8	0.8
Ordinary aluminum alloy window frame	5	160	-	-

On-site measurements were conducted from 16 July to 16 August 2025, with sensor locations shown in Figure 4. Four indoor measurement points were arranged in the living room, south-facing master bedroom, north-facing secondary bedroom, and kitchen, while one outdoor measurement point was installed outside the building. The sensors were positioned 0.95 m above the floor and away from direct solar radiation, localized heat sources, and significant airflow disturbances. Air temperature and relative humidity were recorded at 10 min intervals. During the measurement period, air-conditioning systems, lighting, and major appliances remained switched off, and windows were closed to minimize the influence of occupant behavior and internal heat gains on model calibration. Tinytag temperature–humidity recorders were used over stated ranges of −25 to 85 °C and 0–100% RH with a stated precision of ±2%; building dimensions were checked using a laser range finder with a 0–60 m range and 0.01 m stated precision. The 0.95 m sensor height falls within the 0.70–1.80 m representative occupied-zone range specified in JGJ/T 132-2009.

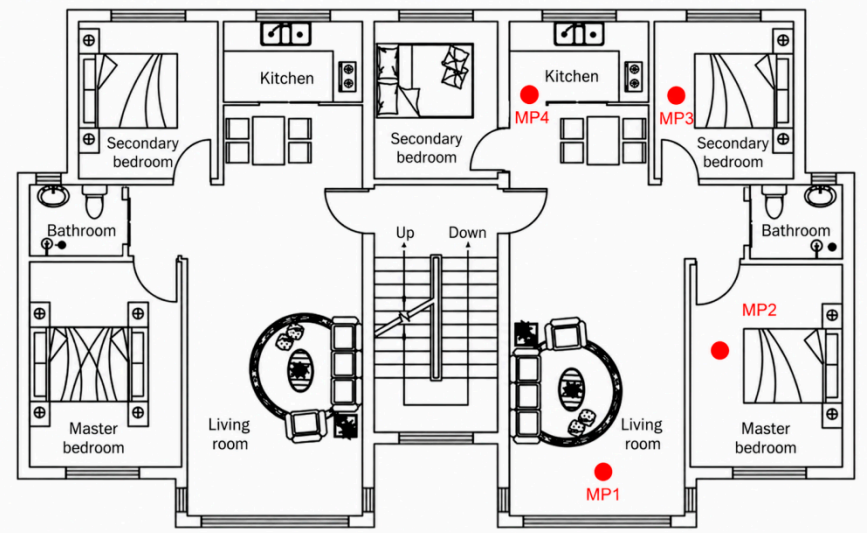


Figure 4. Layout of on-site measurement points.

Model calibration was performed using normalized mean bias error (NMBE) and coefficient of variation of the root mean square error [CV(RMSE)] to evaluate the consistency between simulated and measured values:

$$\mathrm{NMBE} = \frac{\sum_{i=1}^{n}(S_i - M_i)}{(n-p)\bar{M}} \times 100\% \tag{10}$$

$$\mathrm{CV(RMSE)} = \frac{\sqrt{\frac{\sum_{i=1}^{n}(S_i - M_i)^2}{n-p}}}{\bar{M}} \times 100\% \tag{11}$$

where S_i and M_i represent the simulated and measured values at the i-th timestep, respectively; $\bar{M}$ represents the average measured value; n represents the number of data points; and p represents the number of calibrated parameters. In this study, $|\mathrm{NMBE}| < 10\%$ and $\mathrm{CV(RMSE)} < 20\%$ were adopted as acceptable calibration criteria. During calibration, input parameters with relatively high uncertainty identified from the field survey were adjusted, while the remaining simulation boundaries were fixed after calibration.

3.3. Parametric Simulation and Data Generation

After calibration of the baseline model, the IDF file exported from DesignBuilder was imported into JEPlus, with EnergyPlus used as the batch simulation engine. JEPlus employed parameter identifiers to replace target fields, allowing different parameter combinations to be automatically simulated under identical weather conditions, operating schedules, and system boundaries. This ensured consistency in the underlying computational logic among the baseline model, parametric simulations, and re-simulation validation.

The final variable system was determined based on sensitivity analysis results and engineering interpretability requirements. Among the initial variables, the thermal conductivity of planting substrate exhibited limited influence on ANEUI and DH and was therefore excluded from subsequent optimization following the classification criterion defined in Section 2.2.3. Window height and window widths in different orientations were converted into WWRs for the south, north, east, and west orientations. After adjustment, the optimization model still contained 26 variables, with detailed ranges presented in Table 1.

Latin hypercube sampling (LHS) was employed to generate 5000 parameter combinations within the 26-dimensional variable space [28]. Continuous variables were sampled within their predefined boundaries, while discrete variables were mapped to specified levels.

Each parameter combination corresponded to one annual EnergyPlus simulation, producing cooling, heating, lighting, and equipment electricity consumption, rooftop photovoltaic generation, and thermal comfort outputs at each simulation timestep. For each simulation case, the PMV results were post-processed using the DH definition given in Section 2.2.1. The resulting annual DH value was then used as the target output for training the DH surrogate model. ANEUI was calculated from the annual energy-use and photovoltaic-generation results, whereas IRC was independently calculated using the engineering quantity–unit cost model.

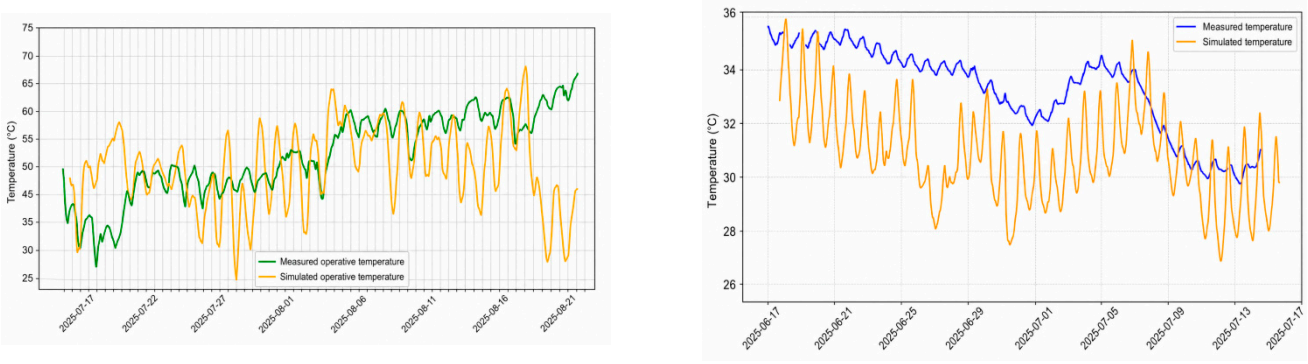
The 26 input variables and three output indicators (ANEUI, DH, and IRC) were integrated according to sample IDs to form the dataset for ANN training and testing. The dataset was subsequently randomly shuffled, normalized, and divided according to the proportions described in Section 2.3.

4. Results and Discussion

4.1. Model Calibration and Sensitivity Analysis

4.1.1. Model Calibration

The comparison between measured and simulated values is presented in Figure 5. The model reproduced the overall variation trends of indoor air temperature and relative humidity during the measurement period, including diurnal fluctuations and differences among rooms. Local deviations may have resulted from factors that are difficult to fully parameterize, such as occupant behavior, local shading conditions, indoor thermal storage, and actual air infiltration. However, no persistent systematic overestimation or underestimation was observed. The measured data underlying this comparison are summarized in Table A1 and Figure A2: indoor mean temperatures ranged from 33.00 to 33.71 °C with diurnal ranges of 5.15–6.67 °C, against 32.18 °C and 20.47 °C at the outdoor reference point, so the indoor environment was strongly damped relative to outdoor conditions.



(a) (b)

Figure 5. (**a**) Comparison between measured and simulated relative humidity; (**b**) Comparison between measured and simulated air temperature.

The two calibration error indicators were 9.6% and 18.4%, respectively, both below the predefined criteria of $|NMBE| < 10\%$ and $CV(RMSE) < 20\%$. The field measurements covered only one summer month, and the calibration simulation used a typical meteorological year weather file rather than the measured hourly weather data during the test period. Therefore, the calibration errors reflect both model-related discrepancies and differences between the actual and TMY weather sequences. The same TMY weather file was used for the 5000 annual simulation samples and subsequent optimization cases to ensure internal comparability among retrofit alternatives; however, the resulting annual performance

should be interpreted as a conditional comparison under the adopted TMY boundary rather than as independently validated annual performance.

4.1.2. Morris Sensitivity-Analysis Results

The results of the Morris sensitivity analysis are shown in Figure 6. The heating setpoint temperature, window U-values in the south and north orientations, insulation thickness of several oriented external walls, and air infiltration rate exhibited relatively high overall effects on ANEUI or DH. The heating setpoint temperature directly determines the indoor-outdoor temperature difference and heating demand during winter, while also affecting the duration of PMV exceedance. Therefore, it influences both energy performance and thermal comfort objectives.

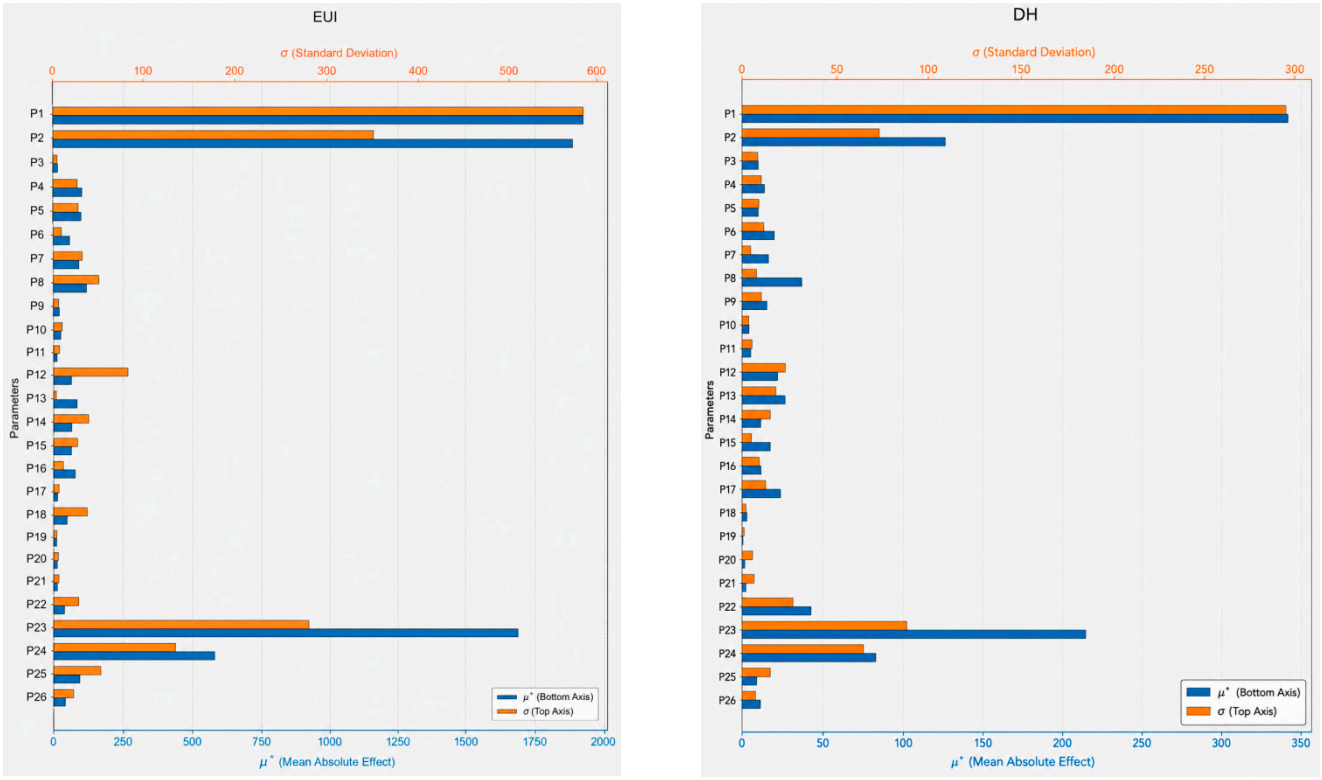


Figure 6. Morris sensitivity analysis results: (**a**) ANEUI; (**b**) DH. Blue bars denote the mean absolute elementary effect (μ*) and orange bars denote the standard deviation (σ) of the elementary effects. The definitions of P1–P26 are provided in Table 1.

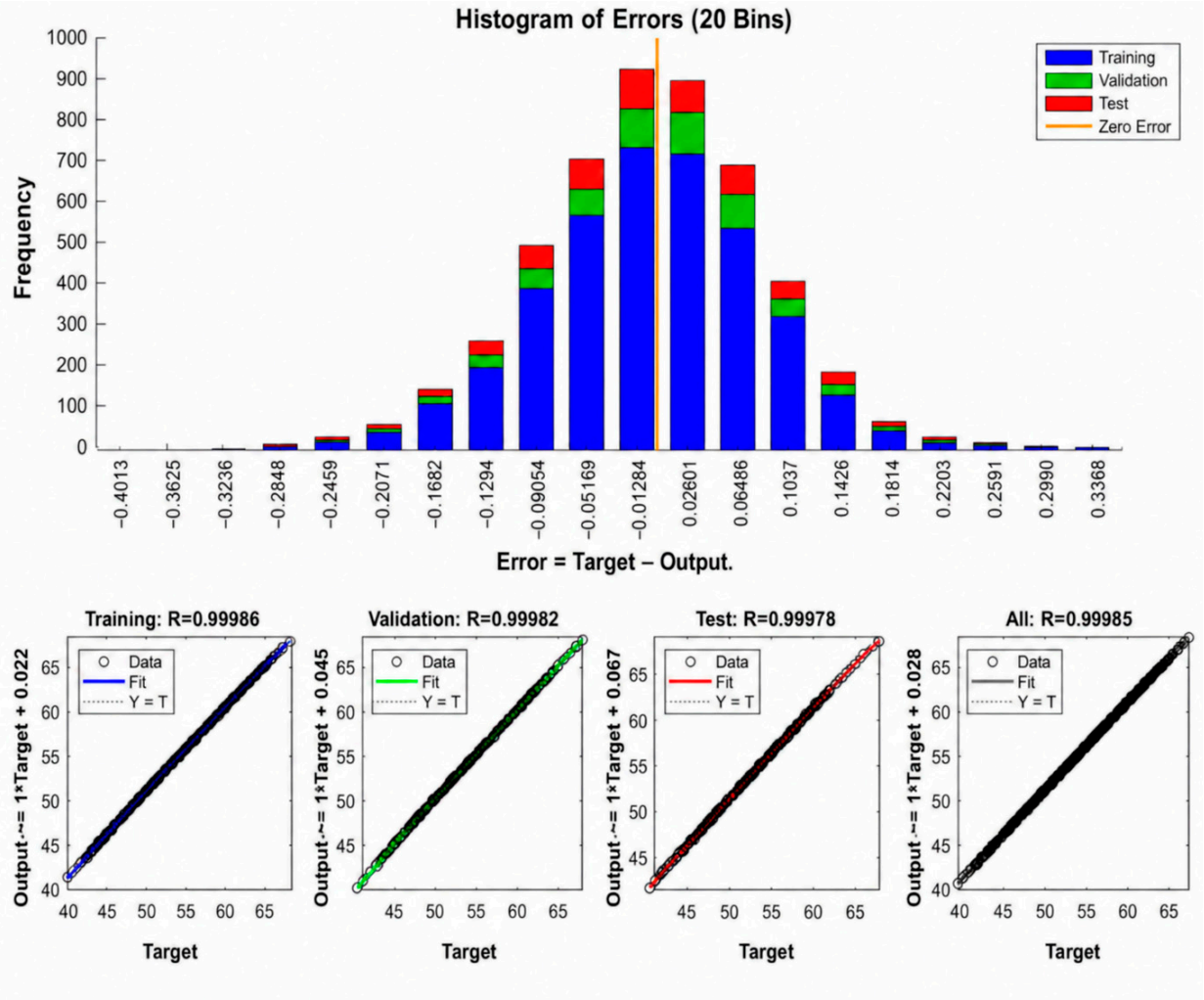
The sensitivity of south- and north-facing window U-values is related to the relatively weak thermal performance of the transparent building envelope in the case building. Window heat transfer not only increases winter heat loss but also affects the inner surface temperature of windows and human radiant heat exchange, thereby influencing both ANEUI and DH.

The insulation-related parameters exhibited certain orientation-dependent differences. The insulation thickness of south and west walls had relatively higher impacts on ANEUI, indicating that envelope heat transfer is jointly affected by solar radiation and orientation-related boundary conditions. Air infiltration rate and external shading depth showed relatively strong effects on DH. The former alters indoor heat balance through uncontrolled air exchange, while the latter influences summer overheating by regulating solar heat gains. Therefore, thermal comfort is not determined solely by steady-state heat transfer

through the building envelope, but is also affected by infiltration ventilation and solar radiation control. In contrast, the sensitivities of plant layer solar absorptance and planting substrate thermal conductivity were relatively low. These parameters mainly modify local heat transfer processes within or at the surface of the green envelope system, and their effects were weaker than those of variables directly influencing building loads, such as temperature control, window heat transfer, wall insulation, and air infiltration. Based on these findings, retrofit strategies should prioritize windows, airtightness, and major thermal weak points. Low-sensitivity measures such as vertical greening should be evaluated considering landscape improvement, surface shading, and maintenance requirements rather than only energy-saving performance.

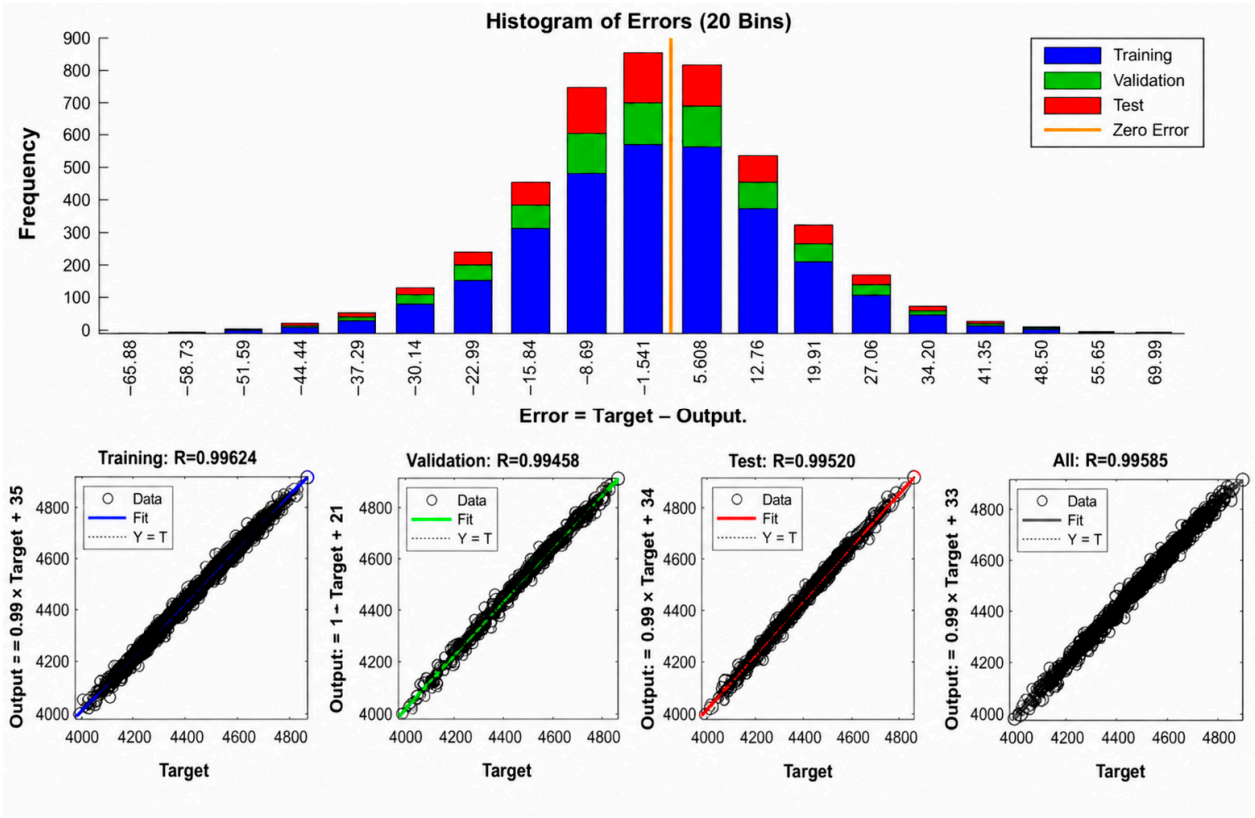
4.2. ANN Prediction Performance

The test-set performance indicators of the three ANN models are summarized in Table 8, and the residual distributions and regression results are shown in Figure 7. The ANEUI and DH models achieved relatively lower prediction errors, whereas the IRC model showed comparatively higher errors.

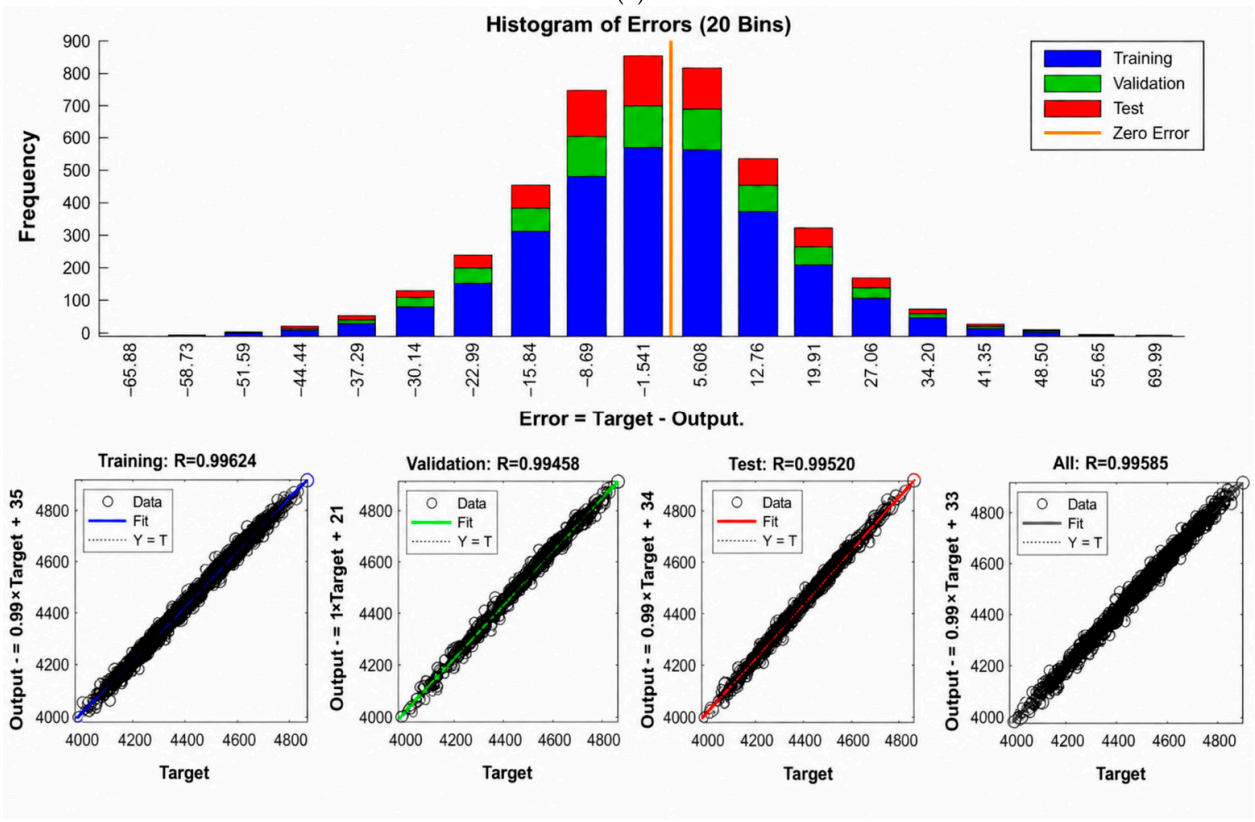


(a)

Figure 7. *Cont.*



(b)



(c)

Figure 7. (**a**) Residual Distribution and Regression Results for ANEUI; (**b**) DH Residual Distribution and Regression Results; (**c**) IRC Residual Distribution and Regression Results.

Table 8. Test-set performance of ANN surrogate models.

Evaluation Metric	ANEUI	DH	IRC
Coefficient of determination (R^2)	0.9996	0.9943	0.9237
Mean squared error (MSE)	0.00899	328.64	1940.72
Root mean squared error (RMSE)	0.0948	18.13	44.05
Mean absolute percentage error (MAPE)	0.18%	0.40%	9.24%

The ANEUI model achieved an R^2 of 0.9996 and a MAPE of 0.18%, while the DH model achieved an R^2 of 0.9943 and a MAPE of 0.40%. The predicted values of both models showed good agreement with the simulation results. The residuals were mainly distributed around zero, without obvious systematic deviations that increased with the target value. This indicates that ANN can effectively represent the nonlinear relationship between high-dimensional retrofit variables and annual net energy use and annual thermal discomfort duration.

The IRC model achieved an R^2 of 0.9237 and a MAPE of 9.24%, showing lower prediction performance than the ANEUI and DH models. ANEUI and DH are derived from continuous building thermal processes, resulting in relatively smooth input-output relationships. In contrast, IRC involves discrete price mappings associated with window performance levels, photovoltaic configurations, and vertical greening types. The stepwise variations and local discontinuities in the cost function increase the difficulty of fitting a continuous surrogate model.

The ANEUI and DH models were suitable for rapid performance evaluation during the optimization process, while the IRC model provided indicative cost estimates for the screening of candidate solutions. The initial retrofit cost of the compromise solution was therefore also recalculated from the engineering quantities and the comprehensive unit prices of its components through Equation (3), giving 398.9 CNY/m^2. None of the three surrogate models should be considered a complete replacement for physical simulation or engineering cost estimation.

4.3. Algorithm Comparison and Pareto Trade-Off Analysis

4.3.1. Algorithm Comparison

The three-dimensional Pareto fronts obtained by the three algorithms are presented in Figure 8. The solution set generated by MOPSO was relatively concentrated in the low-IRC region, but its coverage of the objective space was limited. NSGA-III achieved a wider coverage range, although some solutions were relatively distant from the low-objective region. The Pareto front generated by NSGA-III-PSO was generally closer to the region with lower ANEUI, DH, and IRC, showing a better balance between convergence performance and search coverage. The algorithm performance indicators are summarized in Table 9.

Table 9. Performance indicators of the three optimization algorithms.

Optimization Algorithm	HV	SP
NSGA-III	0.1798	0.0466
MOPSO	0.2995	0.0502
NSGA-III-PSO	0.5446	0.0659

HV and SP were computed from a single run of each algorithm under the settings of Table 2. Repeated independent runs were not performed, so run-to-run means and standard deviations are not available and the values are not a measure of algorithmic stability.

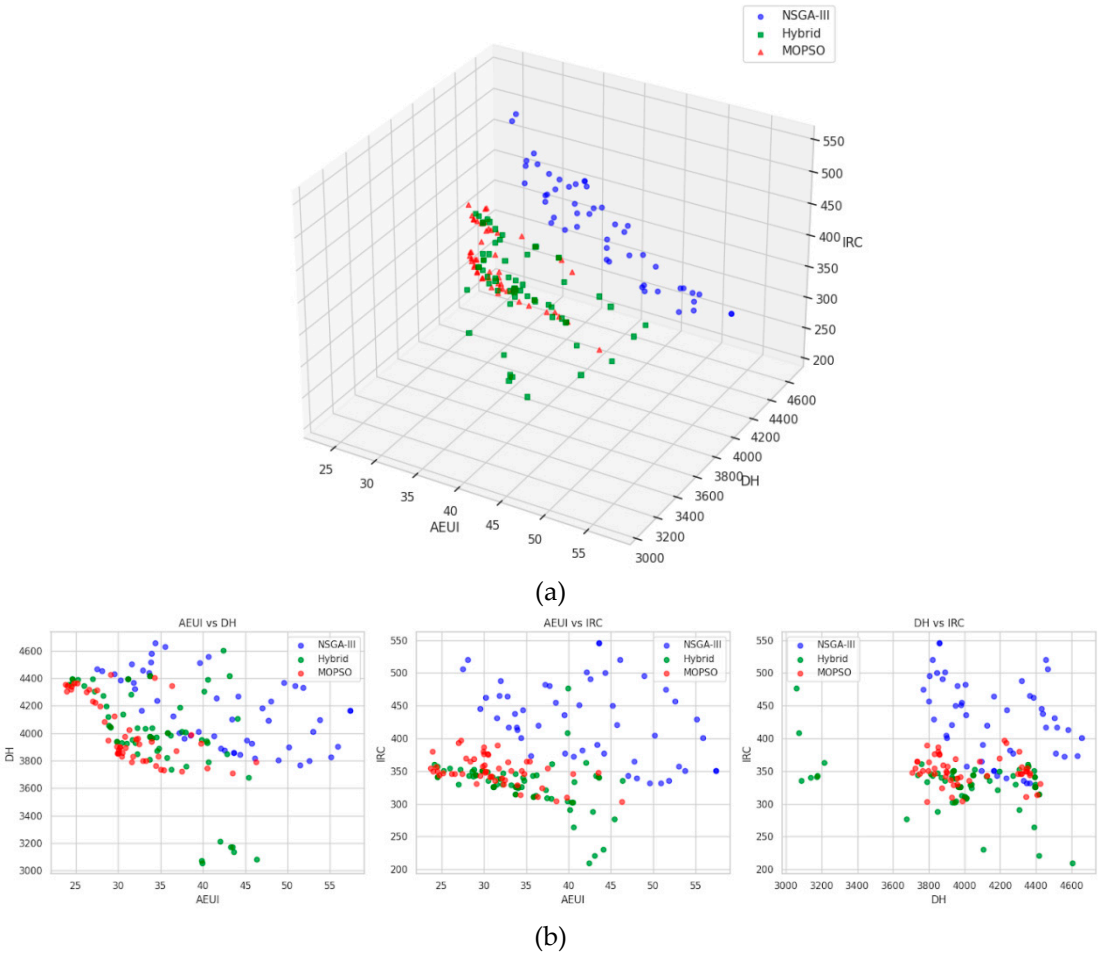


Figure 8. (**a**) Three-dimensional Pareto fronts of the three optimization algorithms; (**b**) ANEUI-DH-IRC spatial distribution of NSGA-III-PSO solutions.

The HV value of NSGA-III-PSO was 0.5446, which was higher than those of MOPSO and NSGA-III, indicating that its non-dominated solution set covered a larger effective objective space. NSGA-III achieved the lowest SP value of 0.0466, suggesting that its solutions were distributed more uniformly. The SP value of NSGA-III-PSO was 0.0659, indicating that some solutions were concentrated toward high-performance regions.

Because the subsequent decision-making process emphasized high-quality solutions close to the ideal region, NSGA-III-PSO was adopted to generate the Pareto candidate set. However, if maintaining continuous and uniformly distributed solution spaces is prioritized, NSGA-III still provides comparative advantages.

4.3.2. Objective Trade-Offs

The Pareto solution set obtained by NSGA-III-PSO is presented in Figure 8. Clear nonlinear trade-off relationships were observed among ANEUI, DH, and IRC. The conflict between ANEUI and IRC mainly resulted from the incremental investment required for performance improvement. Reducing window U-values, increasing envelope insulation thickness, and increasing rooftop photovoltaic coverage can reduce annual net energy use, but these measures simultaneously increase material, component, and installation costs. Particularly in the low-ANEUI region, the marginal energy-saving benefits obtained from further improving envelope performance gradually decrease, while high photovoltaic coverage still requires additional initial investment. Therefore, further reductions in ANEUI generally require higher marginal costs.

A trade-off also existed between DH and IRC. High-performance windows, reduced air infiltration, and external shading can improve interior surface temperatures, reduce uncontrolled heat exchange, and mitigate summer solar heat gains, thereby reducing discomfort hours. However, these measures also increase retrofit investment. Meanwhile, some passive measures can simultaneously reduce energy use and discomfort hours, meaning that DH and IRC do not exhibit a strictly monotonic relationship but instead show segmented characteristics under different parameter combinations.

The relationship between ANEUI and DH involved both synergy and competition. Improvements in insulation, energy-efficient windows, airtightness, and appropriate shading can generally reduce both building loads and discomfort hours. However, stricter indoor temperature control, although beneficial for thermal comfort improvement, may increase cooling or heating demand. Rooftop photovoltaic systems mainly reduce ANEUI by offsetting building electricity consumption and do not directly influence indoor thermal conditions. Therefore, solutions with similar ANEUI values may still exhibit substantially different DH values.

These results indicate that pursuing the minimum energy use, minimum discomfort hours, or minimum retrofit cost independently may lead to significant deterioration in other objectives. The role of the Pareto front is therefore to provide feasible solutions under different preference conditions rather than identify a single absolute optimum solution.

4.4. Compromise Solution and Simulation-Based Performance Assessment

4.4.1. TOPSIS-Based Compromise Solution

The combined subjective-objective weighting TOPSIS method was applied to rank the 50 non-dominated solutions generated by NSGA-III-PSO, and the composite score and final rank of every candidate solution are listed in Table A5. Solution No. 16 obtained the highest relative closeness value of 0.5860 and was ranked first. The combined weights of ANEUI, DH, and IRC were 0.398, 0.447, and 0.156, respectively, indicating that the decision-making process placed slightly greater emphasis on thermal comfort and energy performance than on initial retrofit cost. The selected solution was not the extreme solution of any individual objective. Varying each component of the combined weight vector by factors of 0.8–1.2 produced 121 weight sets; No. 16 ranked first in 72 of them and within the three highest in 87, with the first position passing to No. 39 (28 sets), No. 3 (19) and No. 14 (2). The five highest-ranked solutions differ by no more than 4.2% in ANEUI, 3.0% in DH, and 1.6% in IRC, so the ranking is stable within the near-optimal region of the front but not across the whole weight domain. The retrofit parameters of the compromise solution are presented in Table 10.

Regarding envelope parameters, the compromise solution set the insulation thicknesses of the roof, external walls, and floor at either the lower boundary or intermediate levels of their respective search ranges, rather than simply maximizing all insulation parameters. This indicates that under initial cost constraints, the marginal performance improvement obtained by further increasing insulation thickness could not compensate for the additional material and construction costs. Meanwhile, the air change rate was reduced to 0.5 h^{-1}, and windows with lower U-values were adopted. These measures prioritized the control of two sensitive heat loss pathways: window heat transfer and infiltration losses, which is consistent with the sensitivity analysis results.

Table 10. Retrofit parameters of the TOPSIS-based compromise solution.

Parameter ID	**P1 Cooling Setpoint Temperature (°C)**	**P2 Heating Setpoint Temperature (°C)**	**P3 MW Insulation Thickness (m)**	**P4 North Wall XPS Insulation Thickness (m)**	**P5 South Wall XPS Insulation Thickness (m)**	**P6 West Wall XPS Insulation Thickness (m)**	**P7 East Wall XPS Insulation Thickness (m)**	**P8 Floor XPS Insulation Thickness (m)**
Value	27	23	0.12	0.16	0.14	0.12	0.12	0.05
Parameter ID	P9 North window glass U-value	P10 South window glass U-value	P11 North window glass SHGC	P12 South window glass SHGC	P13 North wall XPS thermal conductivity (W/m·K)	P14 South wall XPS thermal conductivity (W/m·K)	P15 West wall XPS thermal conductivity (W/m·K)	P16 East wall XPS thermal conductivity (W/m·K)
Value	1.6	1.45	0.43	0.6	0.029	0.03	0.029	0.031
Parameter ID	P17 Plant layer solar absorptance	P18 Plant layer thickness (m)	P19 Photo-voltaic tilt angle (°)	P20 Photo-voltaic coverage ratio (%)	P21 Shading depth (m)	P22 Air infiltration rate (h^{-1})	P23 South WWR (%)	P24 North WWR (%)
Value	0.9	0.26	22.3	81.22	0.61	0.5	50	20
Parameter ID	**P25 East WWR (%)**					**P26 West WWR (%)**		
Value	30					16		

The transparent envelope adopted orientation-specific configurations. The north-facing window-to-wall ratio (WWR) was controlled at 20% with low-U-value windows to reduce winter heat losses. The west-facing WWR was set at 16% to mitigate overheating caused by low-angle solar radiation in summer. The south-facing WWR was increased to 50%, combined with fixed external shading with a depth of 0.61 m, achieving a balance among winter solar gains, natural lighting, and summer shading effects. The east-facing WWR was set at 30%. These configurations indicate that a unified WWR cannot effectively respond to different solar radiation conditions and heat transfer boundaries among orientations, while orientation-specific adjustments are more consistent with the thermal response characteristics of the case building. The selected thermal properties were translated into constructible glazing assemblies: the south-facing windows used 6 mm Low-E glass + 12 mm argon + 12 mm Low-E glass ($U = 1.45$ W/(m^2·K), SHGC = 0.60), while the north-facing windows used 6 mm high-transmittance Low-E glass + 12 mm argon + 6 mm clear glass with thermally broken aluminum frames ($U = 1.60$ W/(m^2·K), SHGC = 0.43).

The selected compromise solution adopted a rooftop photovoltaic coverage ratio of 81.22% and an installation tilt angle of 22.3°. Under the net-electricity accounting framework adopted in this study, photovoltaic generation reduced the calculated ANEUI by offsetting part of the building's annual electricity demand. This supply-side offset did not directly reduce the building's heating or cooling loads; therefore, the reduction in ANEUI should not be interpreted as an equivalent reduction in thermal demand. The photovoltaic system also increased the initial retrofit cost, because C_PV in Equation (3) is priced from the unit costs of the configurations listed in Table A4; a higher coverage ratio is therefore obtained at the expense of a higher IRC. Changes in heating and cooling demand and indoor thermal comfort were primarily associated with the envelope, airtightness, shading, and temperature-control parameters, whereas the photovoltaic system mainly affected net electricity use and initial retrofit cost.

Although vertical greening was included in the final retrofit combination, its sensitivity was relatively low. Therefore, it should be regarded primarily as a measure for surface thermal buffering and comprehensive environmental improvement rather than the dominant contributor to energy-saving performance.

Considering the sensitivity analysis results and the characteristics of the compromise solution, the main performance improvements can be attributed to the coordinated effects

of energy-efficient windows, envelope insulation, air infiltration control, orientation-specific WWR configurations, south-facing external shading, and rooftop photovoltaics. Among these measures, windows, insulation, and airtightness reduce building loads from the demand side; shading and orientation-specific glazing regulate solar gains; and photovoltaics reduce net energy use from the supply side.

4.4.2. Comparison of ANN Predictions with EnergyPlus Re-Simulation Results

The ANN-predicted ANEUI was 34.79 kWh/(m^2·a), while the EnergyPlus re-simulation result was 35.98 kWh/(m^2·a), representing a 40.3% reduction compared with the simulated baseline. The relative error between the two results was 3.31%. DH decreased from 5413.2 h for the simulated baseline to 4012.5 h based on the re-simulation result, corresponding to a reduction of 25.8%. The relative error between ANN prediction and re-simulation was 1.83%. The ANN predictions and re-simulation results are presented in Table 11.

Table 11. ANN predictions and re-simulation results of the compromise solution.

Objective	Baseline Building	ANN Prediction After Retrofit	EnergyPlus Re-Simulation After Retrofit	Improvement Compared with Baseline (%)
ANEUI	60.29 kWh/(m^2·a)	34.79 kWh/(m^2·a)	35.98 kWh/(m^2·a)	40.3%
Building-side electricity demand	60.29 kWh/(m^2·a)	—	45.22 kWh/(m^2·a)	25.0%
Rooftop photovoltaic generation	0 kWh/(m^2·a)	—	9.24 kWh/(m^2·a)	—
DH	5413.2 h	3939.2 h	4012.5 h	25.8%

Both surrogate predictions were lower than the re-simulation results. The initial retrofit cost can instead be recomputed directly from Equation (3), so the verification was extended in the cost dimension to four representative solutions covering the extremes of the three objectives (Table 12); the deviations of the four solutions range from −5.7% to +6.0%. The physical re-simulation itself remains limited to the compromise solution, and the costs reported for the four solutions in Table 12 are those recomputed from Equation (3).

Table 12. ANN predictions and recomputed costs of four representative solutions.

Solution (Role)	ANEUI, ANN [kWh/(m^2·a)]	DH, ANN [h]	IRC, ANN [CNY/m^2]	IRC, Equation (3) [CNY/m^2]	εIRC (%)
16 (compromise)	34.79	3939.2	380.54	398.9	−4.6
39 (min. ANEUI)	29.15	4356.2	390.2	414.0	−5.7
3 (min. DH)	44.91	3058.3	231.8	236.4	−1.9
24 (min. IRC)	47.40	4604.6	240.2	226.6	+6.0

IRC cannot be physically validated through EnergyPlus simulation. The initial retrofit cost reported here, 398.9 CNY/m^2, was obtained from the engineering quantities and the categorized unit prices of the compromise solution through Equation (3); the corresponding ANN prediction is 380.54 CNY/m^2, 4.6% lower. It does not include operational energy costs, maintenance, replacement costs, or financial discounting.

4.5. Engineering Implications and Research Limitations

4.5.1. Engineering Implications

The sensitivity analysis, Pareto trade-off analysis, and compromise solution collectively indicate that retrofit strategies for existing multi-story residential buildings should follow the principles of prioritizing critical heat loss pathways, adopting orientation-specific façade configurations, and coordinating demand-side and supply-side measures.

Under limited budgets, improvements should first focus on windows, air infiltration control, and major thermal weak points. Subsequently, window-to-wall ratios, glazing performance, and shading strategies should be adjusted according to orientation-specific solar radiation and heat transfer conditions. Where rooftop conditions permit, photovoltaic systems can be introduced to further reduce building net energy use. Compared with applying the same retrofit intensity to all envelope components, this hierarchical strategy is more effective in controlling initial investment.

Insulation, energy-efficient windows, airtightness improvements, and external shading mainly reduce building loads from the demand side and improve thermal comfort, whereas rooftop photovoltaics reduce electricity consumption from the supply side. Increasing photovoltaic coverage alone cannot directly reduce discomfort hours, while relying only on envelope improvements cannot continuously reduce net energy use. Therefore, these two categories of measures should be coordinated according to project budgets and performance priorities.

In practical applications, a hierarchical decision process consisting of "ANN rapid screening-representative solution re-simulation-engineering cost verification" can improve the efficiency and reliability of multi-objective retrofit decision-making for existing residential buildings.

ANN surrogate models are suitable for large-scale candidate solution screening during the early retrofit design stage [29]. However, their validity is constrained by the boundaries of training samples. Therefore, the final solution still requires physical model re-simulation and engineering feasibility verification. In addition, the economic objective considered in this study represents only the initial retrofit cost. This initial-cost estimate cannot be directly used to evaluate the payback period or life-cycle economic advantage [30].

4.5.2. Research Limitations

Although the regional survey covered five administrative districts and counties of Suzhou, the case analysis was based on only one representative residential building. Therefore, the results cannot fully represent the diversity of existing residential buildings with different construction periods, ownership conditions, and maintenance levels. Application to other climatic regions requires re-calibration of variable ranges and operational boundary conditions.

The baseline model was calibrated using only one month of summer temperature and humidity measurements, without independent validation for winter and transitional seasons. Moreover, calibration was conducted using a typical meteorological year rather than measured hourly weather data during the test period. Deterministic schedules were adopted for occupant opening behavior, air-conditioning operation, room occupancy, and equipment use, which do not fully reflect occupant behavioral randomness. The results therefore represent conditional comparisons under the adopted TMY weather and operating assumptions. Annual energy use, discomfort hours, and the relative performance of retrofit alternatives may differ across weather years or local climatic conditions.

The economic evaluation did not consider energy price fluctuations, photovoltaic revenue, equipment replacement, green maintenance costs, subsidies, or residual value. Physical retrofit implementation and long-term operational monitoring were also not conducted. The selected compromise solution identifies a preferred retrofit configuration within the simulated design space, rather than a construction-ready design. Its rooftop photovoltaic coverage ratio of 81.22% reflects the adopted optimization bounds without explicit constraints on usable roof geometry. Translating this configuration into an implementable design requires a site-specific assessment of structural capacity, usable roof area, and installation requirements, including roof obstructions, maintenance access, parapet

setbacks, shading, and module row spacing at the selected tilt of 22.3°. Since the case building is of brick-concrete construction and its external walls are load-bearing masonry, enlarging the south and east openings requires lintel and ring-beam verification, while the insulation thickened from 0.03 m to 0.12–0.16 m raises anchorage requirements and calls for renewed waterproofing at sills and parapets and for horizontal fire barriers at floor level; the vertical greening is the intensive system of Table A3, whose 0.26 m plant layer adds permanent load and an irrigation requirement to the masonry façade, so it is an optional component, and disturbance to occupied apartments during construction was not modeled.

5. Conclusions

This study investigated the coordinated optimization of energy performance, thermal comfort, and initial retrofit cost for an existing multi-story residential building in Suzhou, Anhui Province. The main conclusions are summarized as follows.

1. Calibrated using one month of measured summer data, the baseline model reproduced the indoor temperature and relative humidity variations of the case building within an acceptable error range and provided a consistent basis for comparing the retrofit alternatives. Morris sensitivity analysis indicated that the heating setpoint temperature, south- and north-facing window U-values, air infiltration rate, and insulation thickness of several oriented walls were the major variables affecting ANEUI and DH. Therefore, retrofit strategies should prioritize windows, airtightness improvement, and major thermal weak points.
2. The ANN models trained using 5000 parameterized samples successfully characterized the nonlinear relationships between retrofit variables and the three optimization objectives. The R^2 values of the ANEUI and DH models were 0.9996 and 0.9943, with MAPE values of 0.18% and 0.40%, respectively. The IRC model achieved an R^2 of 0.9237 and a MAPE of 9.24%. The cost model was suitable for rapid estimation during the optimization process, while the final investment still requires calculation based on engineering quantities and comprehensive unit prices.
3. NSGA-III, MOPSO, and NSGA-III-PSO all generated three-objective Pareto non-dominated solutions. NSGA-III-PSO achieved an HV value of 0.5446 and showed a better balance between convergence performance and objective-space coverage, whereas NSGA-III obtained the lowest SP value of 0.0466, indicating a more uniform solution distribution. The Pareto results demonstrated that ANEUI, DH, and IRC cannot simultaneously reach their respective minimum values, and trade-offs among energy performance, thermal comfort, and investment should be determined according to decision-making preferences.
4. After EnergyPlus re-simulation of the compromise solution, the compromise solution selected by the combined subjective-objective weighting TOPSIS method reduced ANEUI from 60.29 to 35.98 kWh/(m^2·a), representing a reduction of 40.3%; DH decreased from 5413.2 to 4012.5 h, corresponding to a reduction of 25.8%; and IRC was 398.9 CNY/m^2. The ANN prediction errors for ANEUI and DH were 3.31% and 1.83%, respectively. The comprehensive performance improvement was achieved through coordinated measures including orientation-specific window-to-wall ratios, envelope insulation, Low-E windows, south-facing external shading, reduced air infiltration, and high-coverage rooftop photovoltaics.

The results indicate that ANN-assisted multi-objective optimization can identify the trade-offs among energy performance, thermal comfort, and initial investment for existing multi-story residential building retrofits with relatively low computational costs. The proposed framework provides a quantitative reference for retrofit scheme selection in

Suzhou and comparable cold climate regions. However, practical applications should further consider structural safety, construction conditions, occupant behavior, long-term operation and maintenance, and energy price variations. Pareto solutions require additional engineering verification, and a single compromise solution should not be regarded as a fixed solution applicable to all projects.

Author Contributions: Conceptualization, Z.D. and L.W.; methodology, Z.D., S.H. and L.W.; software, S.H.; validation, S.H.; formal analysis, S.H.; investigation, Z.D., S.H. and Z.H.; resources, Z.H. and L.W.; data curation, S.H.; writing—original draft preparation, S.H.; writing—review and editing, Z.D., S.H., Z.H. and L.W.; visualization, Z.D. and S.H.; supervision, L.W.; project administration, L.W.; funding acquisition, L.W. All authors have read and agreed to the published version of the manuscript.

Funding: This research was funded by the China University of Mining and Technology Graduate Innovation Program Project Fund, grant number 2025WLJCRCZL319. The APC was funded by the authors.

Data Availability Statement: The data supporting the findings of this study are available from the corresponding author upon reasonable request. Data requests should be directed to the corresponding author.

Conflicts of Interest: The authors declare no conflicts of interest. The funders had no role in the design of the study; in the collection, analysis, or interpretation of data; in the writing of the manuscript; or in the decision to publish the results.

Abbreviations

The following abbreviations are used in this manuscript:

ANEUI	Annual net electricity-use intensity
ANN	Artificial neural network
ASHRAE	American Society of Heating, Refrigerating and Air-Conditioning Engineers
CNY	Chinese yuan
CV(RMSE)	Coefficient of variation of the root mean square error
DH	Annual discomfort hours
EE	Elementary effects
EPW	EnergyPlus Weather file
HV	Hypervolume
HVAC	Heating, ventilation, and air conditioning
IDF	Input Data File
IRC	Initial retrofit cost per unit floor area
ISO	International Organization for Standardization
jEPlus	Parametric simulation tool for EnergyPlus
KMO	Kaiser–Meyer–Olkin
LHS	Latin hypercube sampling
MAPE	Mean absolute percentage error
MOPSO	Multi-objective particle swarm optimization
MSE	Mean squared error
NMBE	Normalized mean bias error
NSGA-II	Non-dominated sorting genetic algorithm II
NSGA-III	Non-dominated sorting genetic algorithm III
NSGA-III-PSO	Hybrid NSGA-III–particle swarm optimization
PMV	Predicted mean vote
PPD	Predicted percentage of dissatisfied
RH	Relative humidity
RMSE	Root mean square error
SHGC	Solar heat gain coefficient
SP	Spacing

TMY	Typical meteorological year
TOPSIS	Technique for Order Preference by Similarity to Ideal Solution
WWR	Window-to-wall ratio
XPS	Extruded polystyrene

Appendix A. Survey and Measurement Data

Table A1. Measured temperature and relative humidity during the test period.

Variable	Measurement Point	Mean	Maximum	Minimum	Diurnal Range
Temperature (°C)	Measurement Point 1	33.01	35.07	29.92	5.15
	Measurement Point 2	33.71	35.06	29.85	6.21
	Measurement Point 3	33.34	36.18	29.51	6.67
	Measurement Point 4	33.00	35.65	29.48	6.17
	Outdoor Measurement Point	32.18	42.80	23.33	20.47
Relative Humidity (%)	Measurement Point 1	62.49	76.60	47.90	28.70
	Measurement Point 2	59.21	76.10	45.80	30.30
	Measurement Point 3	59.94	75.10	43.70	31.40
	Measurement Point 4	62.28	77.40	45.20	32.20
	Outdoor Measurement Point	69.62	81.40	30.20	61.20

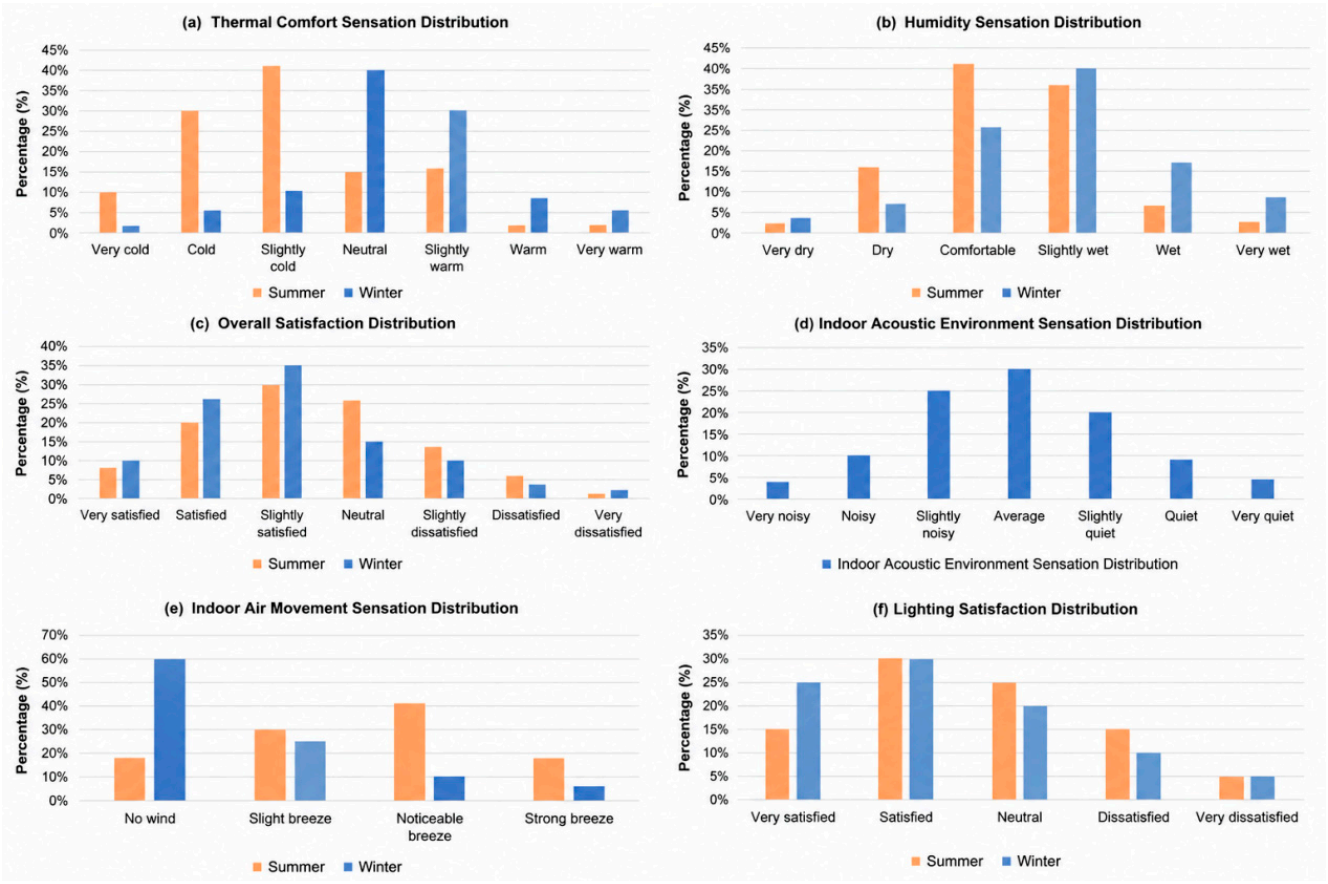
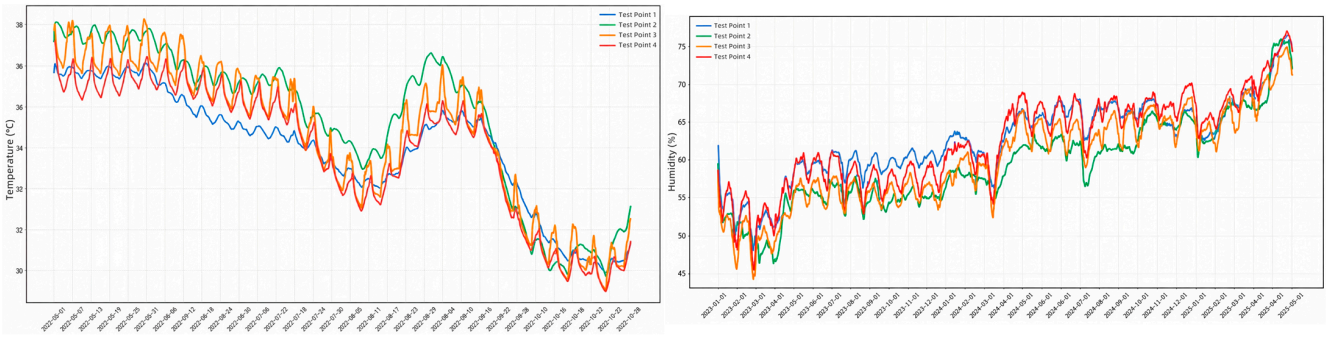


Figure A1. Seasonal distribution of occupants' indoor environmental perceptions and satisfaction.



(a) (b)

Figure A2. Indoor temperature and relative humidity at the measurement points: (**a**) temperature and (**b**) relative humidity.

Appendix B. Simulation Inputs and Cost Parameters

Table A2. Building operating and internal load parameters.

Building Type	Room Type	Air-Conditioned	Winter Relative Humidity (%)	Summer Relative Humidity (%)	Winter Design Temperature (°C)	Summer Design Temperature (°C)	Illuminance (lx)	Lighting Power Density (W/m^2)	Equipment Power Density (W/m^2)
Residential Building	Living Room	Yes	26	65	18	25	300	6.0	9.3
Residential Building	Bedroom	Yes	26	65	18	25	150	6.0	12.7
Residential Building	Dining Room	Yes	26	65	18	25	150	6.0	9.3
Residential Building	Kitchen	No	30	70	—	—	300	6.0	48.2
Residential Building	Bathroom	No	26	70	—	—	150	6.0	0

Table A3. Vertical greening system types and costs.

System Type	Vegetation Layer Thickness (m)	Solar Absorptance	Support Frame Cost (CNY/m^2)	Substrate Layer Cost (CNY/m^2)	Vegetation Cost (CNY/m^2)	Total Vertical Greening System Cost (CNY/m^2)	Corresponding Practical Configuration
Basic	0.05–0.10	0.3–0.5	160–170	45–90	64–107	329–427	Simple mat-based greening system: an ultra-thin substrate planted sparsely with light-colored, drought-tolerant species, such as Sedum lineare.
High-efficiency	0.05–0.10	0.7–0.9	160–170	45–90	150–192	415–512	High-performance modular greening system: a thin, high-performance substrate combined with densely planted, dark-colored vegetation.
Balanced	0.15–0.20	0.5–0.7	180–190	135–180	107–150	482–580	Standard containerized greening system: a medium-depth substrate planted with conventional evergreen herbaceous plants or small shrubs.
Intensive	0.25–0.30	0.7–0.9	200–210	225–270	150–192	635–732	Ecological screening system: a deep substrate combined with multilayered, overlapping, high-biomass dark-colored shrubs.

Table A4. Photovoltaic system configurations and costs.

Photovoltaic Coverage Ratio (PCR)	Installation Tilt Angle, θ (°)	PV Module Cost (CNY/m²)	Corresponding Practical Configuration	Mounting Structure Cost (CNY/m²)	Total PV System Cost per Unit Area (CNY/m²)
20–30%	0–10°	160–240	Low-density roof-mounted array	24–36	184–276
80–85%	0–10°	640–680	Ultra-high-density roof-mounted array	96–102	736–782
40–60%	15–25°	320–480	Inclined-bracket mounting system	72–108	392–588
40–60%	30–60°	320–480	Elevated mounting system	100–150	420–630

Appendix C. ANN and Decision-Making Details

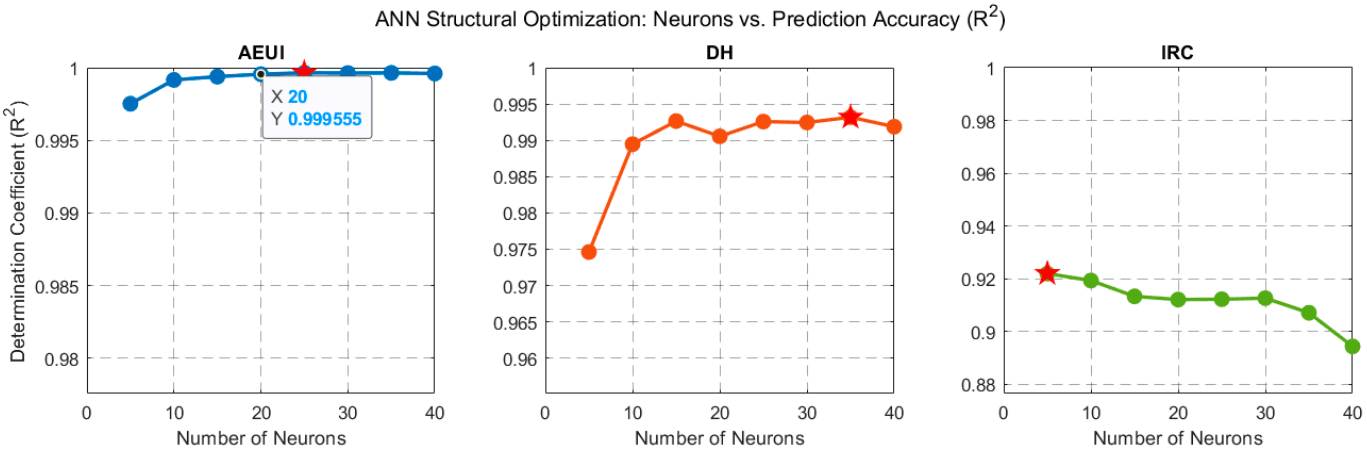
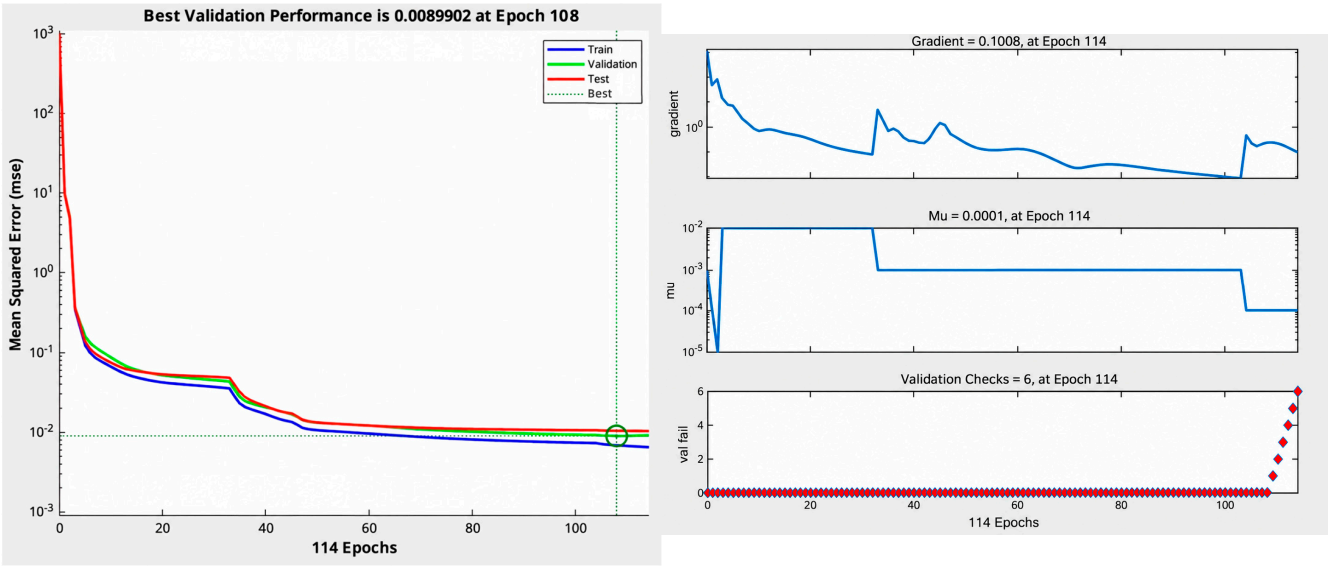


Figure A3. Effect of hidden-neuron number on ANN prediction accuracy.



(a) (b)

Figure A4. *Cont.*

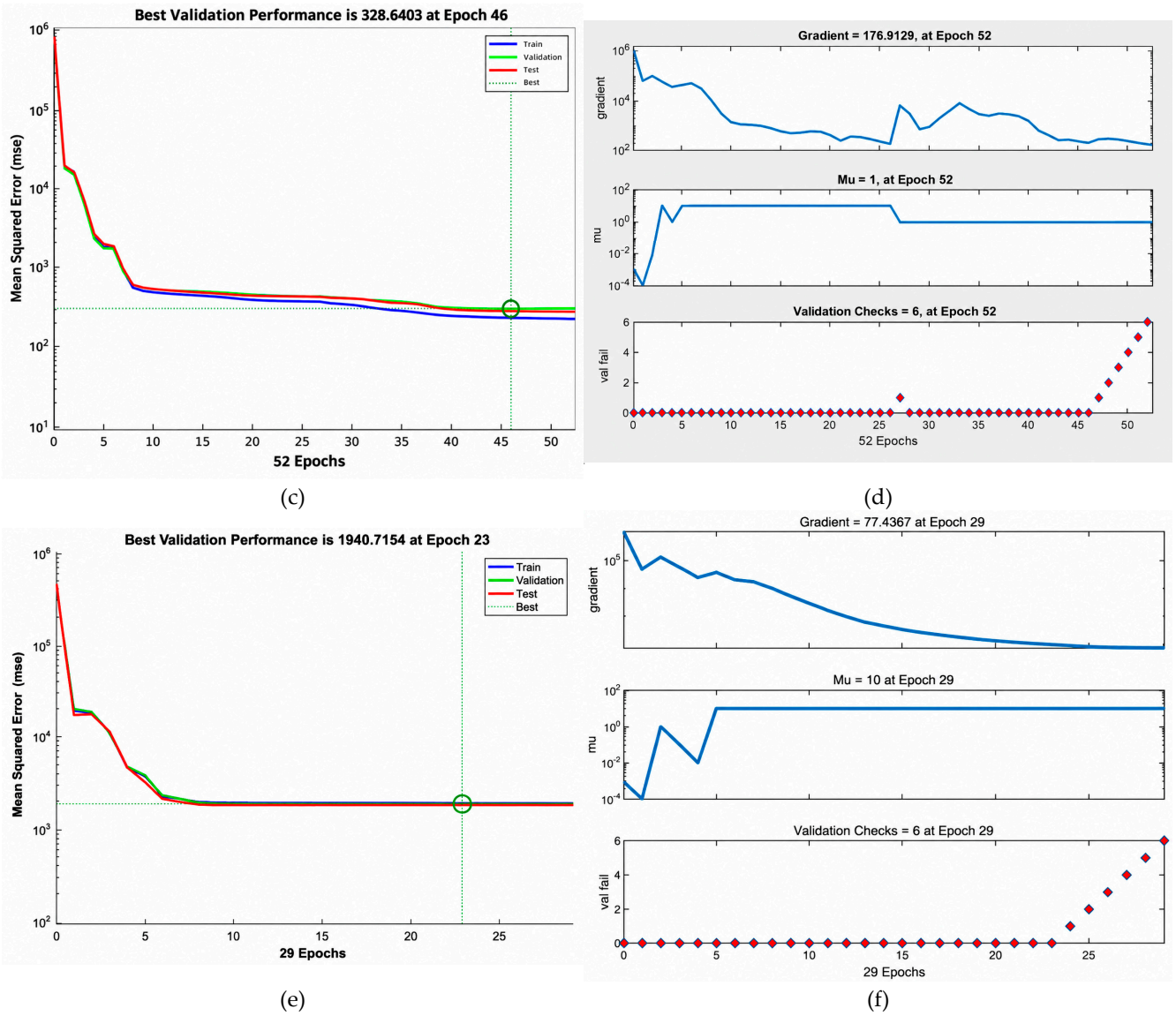


Figure A4. Training performance and learning parameters of the ANEUI, DH, and IRC ANN models: (**a**,**b**) ANEUI; (**c**,**d**) DH; and (**e**,**f**) IRC.

Table A5. TOPSIS ranking results based on combined subjective–objective weights.

Solution No.	Composite Score	Final Rank	Solution No.	Composite Score	Final Rank	Solution No.	Composite Score	Final Rank	Solution No.	Composite Score	Final Rank	Solution No.	Composite Score	Final Rank
1	0.5	21	11	0.46	36	21	0.37	46	31	0.46	34	41	0.56	12
2	0.47	32	12	0.49	26	22	0.49	28	32	0.56	11	42	0.45	37
3	0.52	18	13	0.55	15	23	0.56	10	33	0.31	47	43	0.38	45
4	0.49	25	14	0.49	27	24	0.3	50	34	0.48	30	44	0.5	22
5	0.31	48	15	0.51	20	25	0.59	2	35	0.39	43	45	0.57	8
6	0.3	49	16	0.59	1	26	0.47	33	36	0.4	42	46	0.41	41
7	0.5	23	17	0.42	39	27	0.49	24	37	0.47	31	47	0.58	4
8	0.57	9	18	0.42	38	28	0.55	14	38	0.57	6	48	0.42	40
9	0.58	5	19	0.53	17	29	0.48	29	39	0.57	7	49	0.58	3
10	0.38	44	20	0.55	13	30	0.54	16	40	0.46	35	50	0.51	19

References

1. Ministry of Ecology and Environment of the People's Republic of China. China's Policies and Actions for Addressing Climate Change (2022). Beijing, China, 2022. Available online: https://english.mee.gov.cn/Resources/Reports/reports/202211/P020221110605466439270.pdf (accessed on 14 June 2026).
2. Tettey, U.Y.A.; Gustavsson, L. Energy savings and overheating risk of deep energy renovation of a multi-storey residential building in a cold climate under climate change. *Energy* **2020**, *202*, 117578. [CrossRef]
3. Li, J.; Huang, Y.; Guo, G.; Wu, X. A study on the optimization of energy-saving design for the renovation of old residential buildings in Shanghai. *Archit. J.* **2025**, 13–20. (In Chinese) [CrossRef]
4. Wu, R.; Mavromatidis, G.; Orehounig, K.; Carmeliet, J. Multiobjective optimisation of energy systems and building envelope retrofit in a residential community. *Appl. Energy* **2017**, *190*, 634–649. [CrossRef]
5. Jung, Y.; Heo, Y.; Lee, H. Multi-objective optimization of the multi-story residential building with passive design strategy in South Korea. *Build. Environ.* **2021**, *203*, 108061. [CrossRef]
6. Chegari, B.; Tabaa, M.; Simeu, E.; Moutaouakkil, F.; Medromi, H. Multi-objective optimization of building energy performance and indoor thermal comfort by combining artificial neural networks and metaheuristic algorithms. *Energy Build.* **2021**, *239*, 110839. [CrossRef]
7. Zhai, Y.; Wang, Y.; Huang, Y.; Meng, X. A multi-objective optimization methodology for window design considering energy consumption, thermal environment and visual performance. *Renew. Energy* **2019**, *134*, 1190–1199. [CrossRef]
8. Chen, R.; Tsay, Y.-S.; Ni, S. An integrated framework for multi-objective optimization of building performance: Carbon emissions, thermal comfort, and global cost. *J. Clean. Prod.* **2022**, *359*, 131978. [CrossRef]
9. Wetter, M.; Wright, J.A. A comparison of deterministic and probabilistic optimization algorithms for nonsmooth simulation-based optimization. *Build. Environ.* **2004**, *39*, 989–999. [CrossRef]
10. Futrell, B.J.; Ozelkan, E.C.; Brentrup, D. Optimizing complex building design for annual daylighting performance and evaluation of optimization algorithms. *Energy Build.* **2015**, *92*, 234–245. [CrossRef]
11. García Kerdan, I.; Morillón Gálvez, D. Artificial neural network structure optimisation for accurately prediction of exergy, comfort and life cycle cost performance of a low energy building. *Appl. Energy* **2020**, *280*, 115862. [CrossRef]
12. Mohandes, S.R.; Zhang, X.; Mahdiyar, A. A comprehensive review on the application of artificial neural networks in building energy analysis. *Neurocomputing* **2019**, *340*, 55–75. [CrossRef]
13. Duan, Z.; Wang, L.; Li, B.; Yao, G. Research on multi-objective energy optimization design for multi-story residential buildings in Suzhou region based on artificial neural networks. *Case Stud. Therm. Eng.* **2025**, *73*, 106721. [CrossRef]
14. *ISO 7730:2025*; Ergonomics of the Thermal Environment—Analytical Determination and Interpretation of Thermal Comfort Using Calculation of the PMV and PPD Indices and Local Thermal Comfort Criteria. ISO: Geneva, Switzerland, 2025.
15. Liu, R.; Wang, G.; Deng, Q. Multi-objective optimization of rural residential envelopes in cold regions of China based on performance and economic efficiency. *Case Stud. Therm. Eng.* **2024**, *61*, 104937. [CrossRef]
16. Liu, X.; Chen, Y.; Ge, H.; Fazio, P.; Chen, G. Determination of optimum insulation thickness for building walls with moisture transfer in the hot-summer and cold-winter zone of China. *Energy Build.* **2015**, *109*, 361–368. [CrossRef]
17. Zhan, Y.; Chen, J.; Zeng, L.; Zhou, C.; Wu, Y.; Li, X. Comparative study of different forms of vertical greening on building exterior walls: A case study of Guangzhou. *Guangdong Archit. Civ. Eng.* **2019**, *26*, 6–11. (In Chinese) [CrossRef]
18. Rayegan, S.; Katal, A.; Wang, L.; Zmeureanu, R.; Eicker, U.; Mortezazadeh, M.; Tahmasebi, S. Modeling building energy self-sufficiency using rooftop photovoltaics on an urban scale. *Energy Build.* **2024**, *324*, 114863. [CrossRef]
19. Campolongo, F.; Cariboni, J.; Saltelli, A. An effective screening design for sensitivity analysis of large models. *Environ. Model. Softw.* **2007**, *22*, 1509–1518. [CrossRef]
20. Pianosi, F.; Beven, K.; Freer, J.; Hall, J.W.; Rougier, J.; Stephenson, D.B.; Wagener, T. Sensitivity analysis of environmental models: A systematic review with practical workflow. *Environ. Model. Softw.* **2016**, *79*, 214–232. [CrossRef]
21. Melo, A.P.; Cóstola, D.; Lamberts, R.; Hensen, J.L.M. Development of surrogate models using artificial neural networks for building shell energy labelling. *Energy Policy* **2014**, *69*, 457–466. [CrossRef]
22. Chicco, D.; Warrens, M.J.; Jurman, G. The coefficient of determination R-squared is more informative than SMAPE, MAE, MAPE, MSE and RMSE in regression analysis evaluation. *PeerJ Comput. Sci.* **2021**, *7*, e623. [CrossRef] [PubMed]
23. Deb, K.; Jain, H. An evolutionary many-objective optimization algorithm using reference-point-based nondominated sorting approach, Part I: Solving problems with box constraints. *IEEE Trans. Evol. Comput.* **2014**, *18*, 577–601. [CrossRef]
24. Coello Coello, C.A.; Lechuga, M.S. MOPSO: A proposal for multiple objective particle swarm optimization. In Proceedings of the 2002 Congress on Evolutionary Computation, Honolulu, HI, USA, 6–9 May 2002; Volume 2, pp. 1051–1056. [CrossRef]
25. Zitzler, E.; Thiele, L.; Laumanns, M.; Fonseca, C.M.; da Fonseca, V.G. Performance assessment of multiobjective optimizers: An analysis and review. *IEEE Trans. Evol. Comput.* **2003**, *7*, 117–132. [CrossRef]

26. Ferdous, J.; Bensebaa, F.; Milani, A.S.; Awasthi, A. Development of a generic decision tree for the integration of multi-criteria decision-making and multi-objective optimization methods under uncertainty to facilitate sustainability assessment: A methodical review. *Sustainability* **2024**, *16*, 2684. [CrossRef]
27. Hwang, C.-L.; Yoon, K. *Multiple Attribute Decision Making: Methods and Applications—A State-of-the-Art Survey*; Lecture Notes in Economics and Mathematical Systems; Springer: Berlin/Heidelberg, Germany, 1981; Volume 186. [CrossRef]
28. Shields, M.D.; Zhang, J. The generalization of Latin hypercube sampling. *Reliab. Eng. Syst. Saf.* **2016**, *148*, 96–108. [CrossRef]
29. Ascione, F.; Bianco, N.; De Stasio, C.; Mauro, G.M.; Vanoli, G.P. CASA, cost-optimal analysis by multi-objective optimisation and artificial neural networks: A new framework for the robust assessment of cost-optimal energy retrofit, feasible for any building. *Energy Build.* **2017**, *146*, 200–219. [CrossRef]
30. Yuan, Z.; Zhou, J.; Qiao, Y.; Zhang, Y.; Liu, D.; Zhu, H. BIM-VE-based optimization of green building envelope from the perspective of both energy saving and life cycle cost. *Sustainability* **2020**, *12*, 7862. [CrossRef]

Disclaimer/Publisher's Note: The statements, opinions and data contained in all publications are solely those of the individual author(s) and contributor(s) and not of MDPI and/or the editor(s). MDPI and/or the editor(s) disclaim responsibility for any injury to people or property resulting from any ideas, methods, instructions or products referred to in the content.